DEPARTMENT OF PHYSICS
UNIVERSITY OF JYVÄSKYLÄ
RESEARCH REPORT No. 7/2003

MODELS FOR QUANTUM DOTS AND RINGS

BY
PEKKA KOSKINEN

Academic Dissertation
for the Degree of
Doctor of Philosophy

To be presented, by permission of the
Faculty of Mathematics and Natural Sciences
of the University of Jyväskylä,
for public examination in Auditorium FYS-1 of the
University of Jyväskylä on November 28, 2003
at 12 o'clock noon

Jyväskylä, Finland
November 2003

ISBN 978-951-39-3145-2
URN:ISBN:978-951-39-3145-2

Preface

This work has been carried out at the Department of Physics in the University of Jyväskylä during the years 2001-2003.

I would like to start by thanking Professor Matti Manninen for his supervision, which was carried out with a sense of purpose and scientific skills. Working with him has been very efficient and educating. I am also very grateful to Professor Ulrich Hohenester for his guidance during my time at the Karl-Franzens-University in Graz in the spring 2002.

I would like to thank Dr. Prosenjit Singha Deo, Dr. Susanne Viefers, Mr. Luca Sapienza and Dr. Matti Koskinen for the scientific collaboration. I greatly appreciate to have studied together with Kirsi Manninen, Kimmo Kärkkäinen, Kari Rytkönen and especially Jari Hyväluoma. Kimmo is also acknowledged for proof reading the manuscript. These persons, among all other people at the department, are the ones that have made this period of my life memorable.

Financial support was mainly provided by the Finnish Science Academy through Vilho, Yrjö and Kalle Väisälä foundation. This support is greatly acknowledged.

Finally, I want to express my gratitude to my parents and my beloved Paulina for all their love and support.

Jyväskylä, November 2003

Pekka Koskinen

Abstract

This Thesis consists of an introductory part and six publications that study simplified models for semiconductor nanostructures. The models themselves, including the tight binding, the Heisenberg and the Hubbard model, are familiar since the birth of quantum mechanics, but in this Thesis their role in the description of quantum dots, quantum dot molecules and quantum rings is studied in more detail. The use of simplified models is justified since exact many-body calculations often get too laborious or complicated for practical purposes.

In the first chapter the idea behind the semiconductor band structure confinement and a general formalism for the models are introduced. In the following chapters each model is explained in turn and studied in suitable nanostructures. The last chapter collects the main results and makes the conclusions.

Though the results were obtained mainly by numerical calculations, they are all of qualitative nature. As the central result of this Thesis we may consider the observation, that in appropriate limits the models mentioned above can represent the underlying physics of various semiconductor nanostructures surprisingly well. The models give qualitatively correct results most often, and as the number of model parameters usually is minimized, one cannot even expect to find quantitative agreement. The tight binding model gives a simple explanation for the spontaneous magnetism of quantum dot lattices and the Hubbard model describes qualitatively the energy spectra and general behaviour of perfect and imperfect narrow quantum rings. The Heisenberg model appears to be intimately related to the description of quantum rings. The Hubbard model can be applied to predict directly experimentally observable quantities in coupled quantum dots. The comparison of the model results has been mainly done with the more sophisticated theoretical many-body calculations.

Author's address Pekka Koskinen
Department of Physics
University of Jyväskylä
Finland

Supervisor Professor Matti Manninen
Department of Physics
University of Jyväskylä
Finland

Reviewers Docent Pekka Pietiläinen
Department of Physical Sciences
University of Oulu
Finland

Professor Jari Kinaret
Department of Applied Physics
Chalmers University of Technology and Göteborg University
Sweden

Opponent Professor François Peeters
Department of Physics
University of Antwerpen
Belgium

Contents

1 Semiconductor Nanostructures and Lattice Models **1**
1.1 Introduction 1
1.2 Semiconductor Band Structure 1
1.3 Semiconductor Nanostructures 3
1.4 Lattice Models 7

2 Quantum Dot Lattices and the Tight Binding Model **11**
2.1 The Tight Binding Model 11
2.2 Quantum Dot Lattices 12
2.3 Tight Binding Model for the Spontaneous Magnetism of Quantum Dot Lattices 14

3 Quantum Rings and the Heisenberg Model **23**
3.1 The Heisenberg Model 23
3.2 Model Hamiltonian for Narrow Quantum Rings 24
3.3 Analysis of the Model Hamiltonian 27

4 Quantum Rings, Coupled Quantum Dots and The Hubbard Model **33**
4.1 The Hubbard Model 33
4.2 Ideal Hubbard Rings 35
4.3 Small, Imperfect Hubbard Rings 40
4.4 Four-Wave Mixing in Coupled Quantum Dots 44

5 Summary and Conclusions **51**

References **53**

1 Semiconductor Nanostructures and Lattice Models

1.1 Introduction

Semiconductor nanostructures are nanometer-scale heterostructures within the bulk semiconductor, and usually act as an electron trap or waveguide. This length-scale has a common contact surface with other sciences beside physics, including chemistry and biology, and this makes nanoscience an interdisciplinary effort. The current massive movement in this branch of science is due to the many promising visions for the use of nanostructures in future technology. One of the main goals in research is to scale the current electronic device down to these extremely small length scales.

Indeed, during the last decade the progress in fabrication and measuring techniques at the nanometer-scale already has made many text-book examples of quantum confinement possible. The experimental scientists are able to accurately reproduce samples that show phenomena characteristic to dynamically low-dimensional electron systems.

It is because of the fact that the confinement energy and the electron-electron interaction may be comparable that makes the physics and experiments challenging and the theory of some nanostructures complex. This complexity calls for simple models that would be able to capture the essential physics, but at the same time would be simple enough to allow an easy analysis. In this Thesis we are trying to study how well lattice models could serve as possible candidates for this mission.

In this chapter we first shortly describe the idea behind the band structure confinement and introduce a few confinement models. At the end of the chapter we derive a general formalism for lattice models and discuss their relevance in the description of nanostructures.

1.2 Semiconductor Band Structure

Despite the spatial smallness of semiconductor nanostructures, they are inherently bulk systems. This is actually very important, because in order to describe the confined

electrons in a simple picture, we need a band structure, which in turn requires the (infinite) bulk.

Conduction electrons moving in an infinite lattice of atoms feel a periodic electrostatic potential, the atomic lattice, which acts as the origin of the band structure. The band structure characterizes collectively the single-particle states and the general behaviour of the electrons moving in the bulk. For example, an electron with a wave vector $\boldsymbol{k}$ has the energy $\epsilon_n(\boldsymbol{k})$, where n is the band-index and the function $\epsilon_n(\boldsymbol{k})$ represents the whole band structure. Without any electron-electron or electron-phonon interactions the state of the system is set by assigning the wave-vectors and band-indices for every electron from the band structure.

Fig.1.1 shows the band structure for fictional substances A and B that might represent, GaAs and $Ga_{1-x}Al_xAs$, say [1]. The most important feature of the band structure is the conduction band minimum, because all the excess electrons end up in the vicinity of that point in the reciprocal space. In particular, the curvature of the conduction band at the minimum defines the effective mass $m^* = \hbar^2(\partial^2\epsilon/\partial k^2)^{-1}$, which determines e.g. the dynamic response of a conduction electron to an accelerating force. In the *effective mass* and *envelope function approximation* the complicated interactions with the crystal are put into the single parameter m^* and the complete electron wave function $\psi(\boldsymbol{r})u(\boldsymbol{r})$ is replaced by the envelope function $\psi(\boldsymbol{r})$, where $u(\boldsymbol{r})$ represents the rapid variations in the scale of the atomic lattice [1]. Within this approximation the conduction electrons can be simply described by forgetting the whole atomic lattice, setting the potential energy to correspond to the conduction band minimum[1], and replacing the electron mass $m \to m^*$.

Not surprisingly, it has turned out to be a fair approximation to use the infinite lattice band structure even for sub-micrometer-scale samples, as long as the conduction electrons still 'feel' the periodicity of the underlying atomic lattice. This is reasonable since the band structure theory has been so successful for real substances and, after all, there is no fundamental difference in the basic principle between a macro-scale and sub-micrometer scale samples; they are both finite.

In the next section we put these approximations to work, describe shortly the principle of quantum confinement and present some model confinement potentials.

[1]Conduction band minimum can be a smoothly varying (in the atomic length scale) function of position.

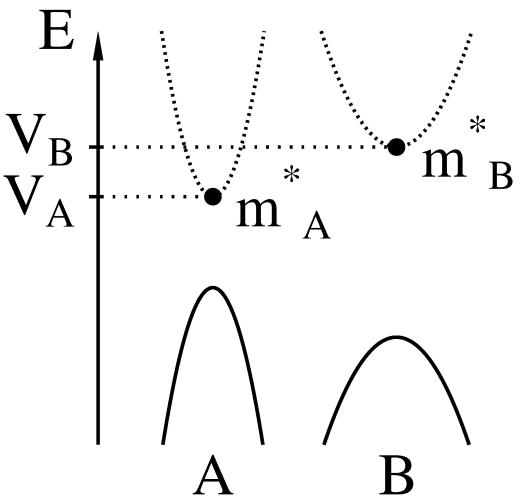

Figure 1.1: The band structures of two fictional substances A and B at the valence and conduction band edges. The conduction electron states can be characterized by knowing the levels of the conduction band minima V_A and V_B, and the effective masses m_A^* and m_B^*.

1.3 Semiconductor Nanostructures

The Two-Dimensional Electron Gas

In Fig.1.1 it was shown how the conduction and valence band edges were related in substances A and B. If pieces of A and B form a junction as in Fig.1.2(a), originally different chemical potentials μ_A and μ_B will adjust themselves by electron transport perpendicular to the interface, until μ is constant throughout the junction. This will result in bending of the band edges [13], and if μ is sufficiently high, the ultimate result may be bound electrons at the interface [2]. The word 'bound' refers only to the perpendicular direction, because in the plane parallel to the junction the electrons are still free to move around, defining the so-called two-dimensional electron gas (2DEG). The two-dimensionality refers to the fact that if the confinement $V(z)$ is sufficiently narrow, the electrons remain at the ground state of the transverse direction, and behave as if they would live in a dynamically two-dimensional world.

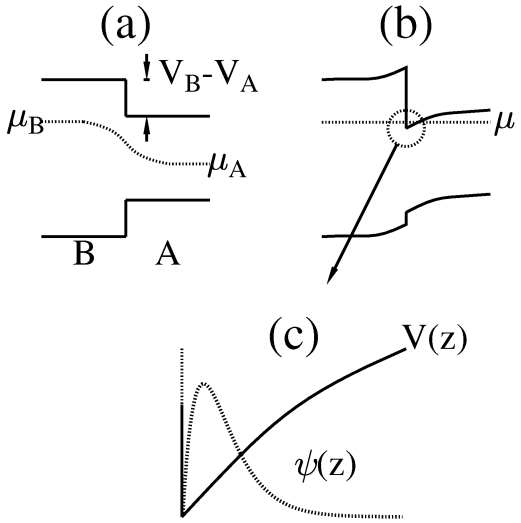

Figure 1.2: A schematic diagram of a junction between substances B and A that have different band gaps, as in Fig.1.1. (a) The band edges before relaxation. (b) Transient transverse electron current makes the chemical potential to level throughout the junction and results in band bending. (c) The conduction band edge at the junction may act as a potential well for the transverse motion of electrons, where the potential form $V(z)$ may have a triangular form. Under appropriate conditions all the electrons confined in the junction will be in the ground state $\psi(z)$ of the transverse direction.

Further Confinement and Model Potentials

The two-dimensional electron gas is considered as the starting point for further electron confinement. If external electrodes are deposited above the 2DEG as in Fig.1.3 e.g. by chemical etching, and a negative voltage is applied, the electrons just below the electrodes are repelled away and the middle region consequently acts as an electron trap confining electrons in all spatial directions. This trap is often called quantum dot (QD). This kind of fabrication allows a good control over the system: the shape and strength of the confining potential can be adjusted by separate gate voltages. Furthermore one can control the number of electrons confined in the structure, and also the current via a voltage difference in source and drain contacts. With similar kind of fabrication processes one can construct coupled quantum dots, quantum dot molecules, quantum dot lattices, quantum rings (QR) etc., almost with the properties one desires [6].

Another technique to fabricate dots and rings is by self-organization, where a thin layer of low band-gap material is deposited above a high band-gap material. If the two materials have a lattice mismatch, the resulting strain in the thin layer may relax

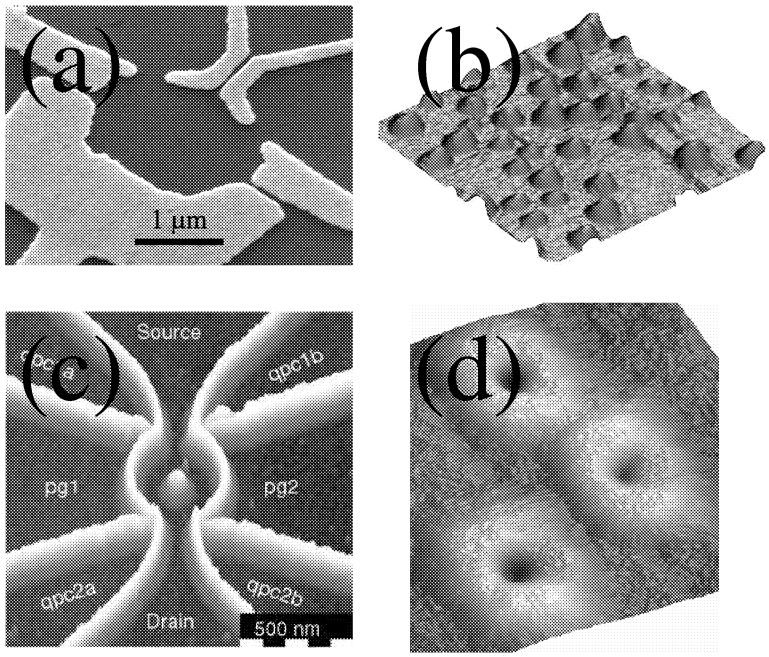

Figure 1.3: Image of a quantum dot (a), an ensemble of self-organized quantum dots (b), quantum ring (c), and a part of an ensemble of self-organized quantum rings. In (a) and (c) the 2DEG is just below the surface and a negative applied voltage depletes electrons below the electrodes and defines an electron trap in the middle region (or in a ring-like region). The current can be controlled by a voltage difference in source and drain contacts, and the potential form by varying gate voltages. In (b) and (d) the self-organizing process creates islands of low band-gap material and these islands trap electrons if the surrounding material has a higher band-gap [18].

and end up forming small dot- or ring-like islands of low band-gap material in the matrix of high band-gap material [6, 16]. These islands can also appear simply because of interface fluctuations at the junction. However, the ultimate consequence is that electrons are trapped in these islands that operate without any externally applied voltages.

As already mentioned, QDs and QRs are formed in electron gas that is dynamically two-dimensional. If the further confinement in the plane is much weaker than the perpendicular confinement, the electrons can be considered moving in strictly two-dimensional xy-plane under a two-dimensional potential $V(x, y)$. The form of V depends much on the particular geometry of the system.

The potential form in the center region of a quantum dot such as the one in Fig.1.3(a) or (b), can be modelled to a first approximation by the harmonic confinement [14]

$$V_{QD}(r) = \frac{1}{2} m^* \omega^2 r^2, \tag{1.1}$$

where $r^2 = x^2 + y^2$, and ω is the confinement strength related to the applied voltage of the repelling electrode or to the geometry of the self-organized dot. Similarly, to a first approximation the potential for a quantum ring is also harmonic [15, 16] and can be written as

$$V_{QR}(r) = \frac{1}{2} m^* \omega^2 (r - R)^2, \tag{1.2}$$

where ω is the radial confinement strength and R is the equilibrium radius arising from the geometry of the ring. Note that the nature of the potential in a quantum dot is always the same whereas in a quantum ring it depends on the relative magnitude of ω and R: At the extremes a QR can be viewed as a QD ($R \to 0$) or as a strictly one-dimensional wire ($\omega \to \infty$).

Artificial Atoms

The general properties of nanostructures can be studied e.g. with capacitance spectroscopy, far-infrared transmission spectroscopy and photoluminescence [15, 16, 17]. Especially quantum rings are frequently studied in magnetic fields, since a number of flux quanta can penetrate the interior of the ring and reveal information about the internal structure via the flux-dependence. In a large ensemble of self-organized nanostructures the distribution in sizes and shapes, as clearly visible Fig.1.3(b), may require an isolation of single dot or ring.

These methods, among others, have shown many characteristic features of nanostructures. As Eq.(1.1) is an attractive potential, just as is the Coulomb potential of an atomic nucleus, QDs share many properties with real atoms. These include the discreteness of the energy spectrum, the shell structure with magic numbers, Hund's rules, and so on. Because QDs can in principle be designed at will, this is why they are also referred to as 'artificial atoms' [19, 20, 21].

In addition of showing properties analogous to real atoms, one can see phenomena such as the Kondo effect, Aharonov-Bohm oscillations in quantum rings with different periodicities and other novel many-body effects. However, many of the phenomena discussed in this Thesis are still waiting for the experimental realization.

What about the applications? The future prospects are quite promising, at least in principle [1, 24, 25, 26, 28, 29, 30]. The information processing techniques today rely entirely on the existence of two-level memory elements, and nanostructures are one of the best candidates for this use in the future. Tuning the spectra of dots or rings might end up having a practical memory device, provided that the coherence time of the two-level system is long enough and that the state can be suitably controlled. One is even

trying to build a quantum computer by exploiting the fact that the system of quantum bits (QUBITs), potentially made of QDs, could be in an entangled superposition of all the possible states. Dots, rings, dot lattices and other structures can be used in lasers and other optical devices, as well as in optoelectronics. In addition they might be used as memory storage or in conventional electronics.

But no matter how promising the application list might look, there is still much theoretical and experimental work to do in order to get a technological revolution at the practical level.

1.4 Lattice Models

In the following we turn our attention to the theoretical description of a *system* of quantum dots. We do this by utilizing the effective mass and envelope function approximations, so that the underlying atomic lattice is forgotten and electrons with mass m^* are described as moving in a smoothly varying external potential[2] $V(\boldsymbol{r})$. The potential might consist e.g. of a multiple number of quantum dot potentials $V(\boldsymbol{r}) = \sum_i V_{QD}(\boldsymbol{r} - \boldsymbol{R}_i)$, where $\boldsymbol{R}_i$ would be the locations of the attractive QDs. For an appropriate description of electrons in these systems, where a strong electron localization near the locations $\boldsymbol{R}_i$ is expected, we pay attention to the general theory of interacting electrons [2, 3].

Derivation of a General Hamiltonian

First of all, the reader should keep in mind that the following derivation is superficial, and it should be read accordingly. On the other hand, its only intention is to merely illustrate the physical approach and the concepts used, so that they would become familiar before discussing the different models in more detail.

Let the single-particle eigenstates of an isolated QD potential $V(\boldsymbol{r}) = V_{QD}(\boldsymbol{r} - \boldsymbol{R}_1)$ be denoted by $\varphi_n(\boldsymbol{r} - \boldsymbol{R}_1)$, i.e. $\hat{h}\varphi_n(\boldsymbol{r}) = \epsilon_n \varphi_n(\boldsymbol{r})$, where $\hat{h} = -(\hbar^2/2m^*)\nabla^2 + V(\boldsymbol{r})$. The eigenstates are localized in the vicinity of the point $\boldsymbol{R}_1$ and they have energies ϵ_n. If we add more QDs centered at $\boldsymbol{R}_2, \boldsymbol{R}_3, \ldots, \boldsymbol{R}_L$, so that all $\boldsymbol{R}_i$'s are well-separated, it is expected that the functions $\varphi_n(\boldsymbol{r} - \boldsymbol{R}_i)$, $i = 1, 2, \ldots, L$ are still fair approximations for the eigenstates of the single-particle Hamiltonian with $V(\boldsymbol{r}) = \sum_{i=1}^{L} V_{QD}(\boldsymbol{r} - \boldsymbol{R}_i)$. In particular, we vaguely assume that functions $\langle \boldsymbol{r} | \boldsymbol{R}_i^n \rangle = \varphi_n(\boldsymbol{r} - \boldsymbol{R}_i)$, $i = 1, 2, \ldots, L$, form approximately a complete low-energy basis set for our system.

[2] By smoothly varying we mean that $V(\boldsymbol{r})$ does not change appreciably in the *atomic* length scale.

The general Hamiltonian describing an interacting N-electron system can be written in the real-space representation as

$$\hat{H} = \sum_i \hat{h}_i + \sum_{i<j} V_C(|\boldsymbol{r}_i - \boldsymbol{r}_j|), \tag{1.3}$$

where the external potential $V(\boldsymbol{r})$ is hidden in $\hat{h}$ as before, and $V_C(r)$ is the mutual Coulomb repulsion between the electrons. In the language of second quantization this turns into

$$\hat{H} = \sum \langle \boldsymbol{R}^n_{i\sigma} | \hat{h} | \boldsymbol{R}^{n'}_{j\sigma'} \rangle c^\dagger_{in\sigma} c_{jn'\sigma'} + \sum V^{nn'mm'}_{ijkl\sigma\sigma'} c^\dagger_{in\sigma} c^\dagger_{jn'\sigma'} c_{km'\sigma'} c_{lm\sigma}, \tag{1.4}$$

where the summations are over all the indices, the operators $c^\dagger_{i,\sigma}$ and $c_{i,\sigma}$ have the usual meaning as the fermionic creation and annihilation operators obeying the anti-commutation relations $\{c_i, c^\dagger_j\} = \delta_{i,j}$ and $\{c_i, c_j\} = \{c^\dagger_i, c^\dagger_j\} = 0$, and where σ represents the spin-index. The matrix elements preceding the c-operators are the usual single and double integrals of the operators in Eq.(1.3) between the given basis states.

Now, since φ's were not exactly the eigenfunctions of $\hat{h}$ in the presence of multiple QDs, the matrix elements of the first term are not diagonal. If $i = j$, $n = n'$ and $\sigma = \sigma'$ the integral will give the expectation value for an electron in the state $|\boldsymbol{R}^n_i\rangle$, which is approximately equal to ϵ_n. On the other hand, if $i \neq j$ the integral will measure essentially the overlap between the states $\varphi_n(\boldsymbol{r} - \boldsymbol{R}_i)$ and $\varphi_n(\boldsymbol{r} - \boldsymbol{R}_j)$. Because of the strong localization of the electrons, the wave-functions do not spill out of the dots very much and we expect the overlap to be considerable only for states that are nearest neighbours. The integral, called the *hopping integral*, can be written for $i \neq j$ schematically as

$$t^{nn'}_{ij} \equiv \langle \boldsymbol{R}^n_{i\sigma} | \hat{h} | \boldsymbol{R}^{n'}_{j\sigma'} \rangle \sim \delta_{\sigma\sigma'} \int \mathrm{d}^3 r \varphi^*_n(\boldsymbol{r} - \boldsymbol{R}_i) \delta V(\boldsymbol{r}) \varphi_{n'}(\boldsymbol{r} - \boldsymbol{R}_j), \tag{1.5}$$

where the local function $\delta V(\boldsymbol{r})$ is just a reminder that what we are computing is actually not a pure overlap, but a somewhat modified one.

The interaction matrix element is responsible for taking the mutual Coulomb repulsion of the electrons into account. If the typical separation between the dots is large, the Coulomb potential is significant only when the electrons occupy the same dot. This reduces the interaction matrix elements into

$$V^{nn'mm'}_{\sigma\sigma'} = (1 - \delta_{nn'}\delta_{\sigma\sigma'}) \int \mathrm{d}^3 r \mathrm{d}^3 r' \varphi^*_n(\boldsymbol{r}) \varphi^*_{n'}(\boldsymbol{r}') V_C(|\boldsymbol{r} - \boldsymbol{r}'|) \varphi_m(\boldsymbol{r}) \varphi_{m'}(\boldsymbol{r}'). \tag{1.6}$$

With the approximations introduced above, Eq.(1.4) can eventually be written as

$$\hat{H} = \sum \epsilon_n c^\dagger_{in\sigma} c_{in\sigma} + \sum_{\langle i,j \rangle} t^{nn'}_{ij} c^\dagger_{in\sigma} c_{jn'\sigma} + \sum V^{nn'mm'}_{\sigma\sigma'} c^\dagger_{in\sigma} c^\dagger_{in'\sigma'} c_{im'\sigma'} c_{im\sigma}, \tag{1.7}$$

with the summations over all the indices. The notation $\langle i, j \rangle$ restricts i and j to be nearest neighbours. The basis set consists of many-electron states (Slater determinants) with all the possible spin- and spatial configurations for the N electrons, where the number of spin-up and -down electrons satisfy $N_\uparrow + N_\downarrow = N$. This is our final result for the Hamiltonian of interacting electrons at the present stage.

Further Considerations

The operator (1.7) can be interpreted as follows. As we are looking at low-energy regime throughout, all the N electrons are localized in the L quantum dots. More generally speaking we could also replace QD potential with any other attracting or localizing potential[3]. If the dots are infinitely far apart, the electrons are purely in the states $|\boldsymbol{R}_i^n\rangle$ and the only contributions come from the on-site energies ϵ_n via the first term in Eq.(1.7) and from the interaction between electrons in the same dot via the last term. If the dots are brought closer together, the states in different dots start to overlap with each other and the Hamiltonian is not diagonal anymore. The electrons sit on different dots, now named *sites*, that may form a molecule, a periodic lattice or whatever geometry, and *hop* from one site to another with spin conservation via the second term in Eq.(1.7).

The Hamiltonian (1.7) is now the branching point for the different models used in this Thesis. Especially the interaction term makes life a bit difficult and therefore requires rough approximations. Constant on-site energy and constant hopping integrals also simplify the system considerably. These different approximations lead to famous models including the tight binding model, the Heisenberg model, the Hubbard model and many others. The basic idea behind these models is nevertheless the same, and in that sense they are fully accounted for by their approximate Hamiltonians derived from Eq.(1.7). In the next three chapters a few of these different approximations are introduced in turn, and applied to various systems of localizing centers.

[3]Especially, as we shall see in Chap.3, the localizing potential can arise from *internal* localization of the electron system without any external potential.

2 Quantum Dot Lattices and the Tight Binding Model

In publication IV of this Thesis we applied the tight binding (TB) model to describe magnetic behaviour of quantum dot lattices. In this chapter we first derive the standard tight binding model and introduce quantum dot lattices shortly. After that we present our modification to the TB model and review the central results that the model yields related to magnetic behaviour of QD lattices.

2.1 The Tight Binding Model

The standard TB model simplifies our starting point, Eq.(1.7) to a compact form. Firstly, we assume a single-particle description, i.e. $N = 1$, and take only one identical state per site. The energy level can then be chosen by setting the on-site energies ϵ_i equal to zero. Secondly, all the nearest-neighbour hopping integrals are set equal and the electron-electron interactions can be neglected altogether since we only have one electron. This is how one ends up with the tight binding Hamiltonian [2, 4]

$$\hat{H} = t \sum_{\langle i,j \rangle \sigma} c^{\dagger}_{i\sigma} c_{j\sigma}. \tag{2.1}$$

This Hamiltonian is one of the standard condensed matter physics text-book approaches for the first calculation of the band structure in a lattice of atoms, for it can be readily solved by taking the Fourier transforms of the creation and annihilation operators [5, 9]. The name 'tight binding' comes from the fact that the electrons are assumed to be tightly bound to the sites, i.e. the spatial extent of the bound electrons is small and the hopping term acts as a small perturbation.

For future use, however, a slightly more general Hamiltonian is needed. The direct interaction term in Eq.(1.7) is still neglected, but some additional consideration is done with the hopping integrals, so that $t_{ij}^{nn'}$ is allowed to have the full dependence on all the indices. Also the on-site energy $\epsilon_n \rightarrow \epsilon_{n\sigma}$ is allowed to depend on the spin although $\hat{h}$ does not show any spin-dependence. Before writing the final Hamiltonian, it is necessary to review certain properties of QD lattices.

2.2 Quantum Dot Lattices

Lattice in a Lattice

One of the main reasons for the excitement over quantum dots is certainly the far-reaching analogy with real atoms. A natural consequence of this analogy is to treat QDs as real atoms: build molecules, clusters and lattices. QD lattice is a superlattice, a periodic construction of quantum dots superimposed in the periodic lattice of atoms. The conduction electrons, treated in the effective mass approximation, feel the periodic superlattice and get another band structure, the *mini-band* structure.

A QD lattice may be formed e.g. by making quantum wires to cross each other, because the effective width of quantum wires at the crossings is larger than the normal width of the wire, and thus the electrons are attracted to these points due to the smaller confinement energy [32]. The formation of a regular QD lattice may also be favored for some self-organizing growth modes while fabricating quantum dots [6]. A highly controllable QD lattice might be manufactured e.g. by simply drilling holes to a large metallic electrode lying on top of 2DEG.

When real atoms form macroscopic crystals, the atomic number, Z, determines the number of electrons and the outermost electron orbital in the system. For a given Z, the Nature adjusts the crystal structure to be FCC, BCC, or something more complicated, and adjusts also the lattice constant to correspond to the equilibrium value. Z also determines the band structure, elasticity and magnetic properties of a crystal. In short, Z determines essentially all the properties of perfect crystals.

With quantum dot lattices the story is different: the confinement is determined by the design of the dots, the lattice constant and symmetry can be adjusted by hand in the fabrication process, the number of electrons per QD may possibly be adjusted by some electrodes lying on the top of the lattice, and that can be even a fractional number. In this sense the macroscopic properties of QD lattices are expected to show rich features. Next we study what happens in particular to the magnetic properties of a QD lattice as we change the number of electrons and the lattice constant at will.

Magnetic Properties

Koskinen *et al.* [31] studied the properties of the magnetic ground state of a QD square lattice with a variable number of electrons per QD and different lattice constants. They used the spin-density functional formalism to determine the ground-state energy of antiferromagnetic (AF) and ferromagnetic (F) configurations and constructed a mag-

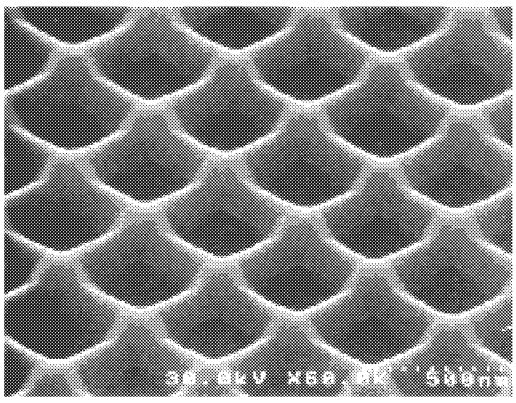

Figure 2.1: Image of a quantum dot lattice [18]. The crossings of quantum wires may provide a larger volume for electrons and thus act as a quantum dot. The wires between the 'dots' may conveniently act as tunneling routes for electrons migrating in the lattice.

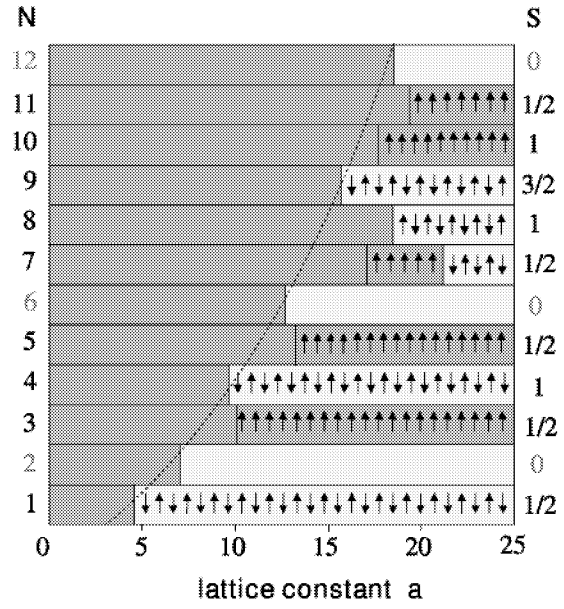

Figure 2.2: The magnetic phase diagram for a QD square lattice [31]. The metallic phase (no band gap) is shown in dark grey and the arrows indicate the magnetic phase (AF=↑↓↑↓, F=↑↑↑↑). N is the (integer) number electrons per quantum dot and S in the right-hand side shows the ground-state spin of an isolated quantum dot.

netic phase diagram as a function of N, the number of electrons per QD, and the lattice constant a. The main features of the phase diagram, shown in Fig.2.2, exhibit systematic behaviour. The system is metallic for a small lattice constant, and the transition to an insulator happens with increasingly large a when N is increased, because of the larger spatial extent of the outer electronic orbitals. The diagram suggests insulating and non-magnetic phase with full shells, insulating and antiferromagnetic phase with half-filled shells, and metallic and ferromagnetic phase with partly filled or nearly full shells. This kind of systematic behaviour suggests that the underlying physics might be quite simple and we ought to search for a model that would explain these properties in a simple way.

2.3 Tight Binding Model for the Spontaneous Magnetism of Quantum Dot Lattices

Magnetism in general is due to exchange interactions between conduction electrons. Since the tight binding model neglects the interactions altogether, the standard model has to be improved if we want to use it for calculating the magnetic properties of QD lattices. For this purpose we review the theory and results of the publication IV.

The Tight Binding Approach

We start by considering a typical low-energy spectrum of an isolated, nearly harmonic QD, as depicted in the left-hand side of Fig.2.3. For generality, we introduce a small anharmonicity for the dot potential, which induces a splitting Δ_{sd} between initially degenerate $2s$ and $1d$-orbitals. The gaps between the shells are still much larger than Δ_{sd}.

If multiple dots form a complete lattice, the magnetic order is expected to develop via the exchange coupling between the nearest neighbours and the coupling is expected to split the originally degenerate spin-states into two. This picture in mind, we *postulate* an exchange splitting Δ, as depicted in Fig.2.3. In ferromagnetic systems the levels are split so that in each dot the lower state has always the same spin, and in antiferromagnetic systems the spin of the lower state alternates from dot to dot. The electrons with a given spin thus feel a dynamically constant exchange potential, and although they are formally treated as non-interacting, the real interactions are effectively taken into account via the exchange splitting.

In the following these ideas are applied in practise using the TB model. First of all, for a square lattice we must use two-site basis as shown in Fig.2.4(c), with the sites

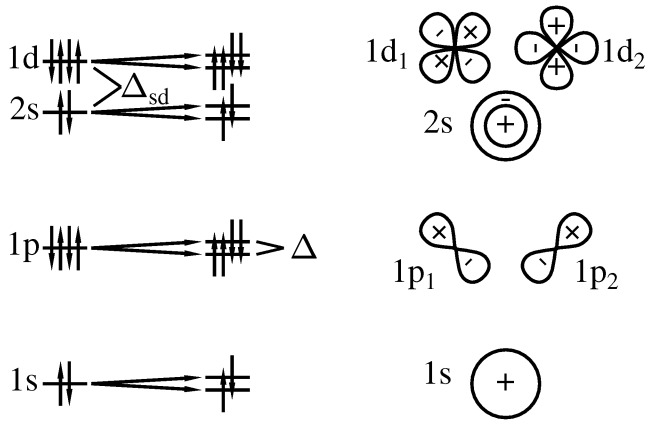

Figure 2.3: The left-hand side shows the level structure of an isolated, slightly anharmonic, two-dimensional QD. Δ_{sd} is the splitting introduced by a small anharmonicity in the dot potential. As the isolated dots approach each other so that the lattice constant is reduced from infinity, the exchange interaction Δ splits the originally degenerate spin-levels. The arrows indicate the spin of the state. The right-hand side shows schematically the basic symmetries of the states.

denoted by a and b. Fig.2.4(a) and (b) shows the ferro- and antiferromagnetic level schemes for sites a and b in the presence of the postulated exchange splitting.

The on-site energies for the electrons with different spins are now set, but the hopping integrals require some further attention. Eq.(1.5) tells that t's are the overlap integrals between the different orbitals, for which the right-hand side of Fig.2.3 shows the basic symmetries. From these it is quite easy to see which hopping integrals are zero by symmetry. For example, the hopping is forbidden between $1p_1$ and $1p_2$ orbitals in a square lattice. For allowed hoppings the value of t may be different, but the exact evaluation of the integrals is not appropriate because of the vagueness of the postulated exchange splitting Δ. Hence as a first approximation all the different overlap integrals, unless exactly zero by symmetry, are assigned the same value t, the magnitude of which is indirectly related to the lattice constant via the definition (1.5); smaller value of t corresponds to larger lattice constant.

We can now write the model Hamiltonian for a *given* spin as

$$\hat{H} = \sum_{i,n}(\epsilon_n^a a_i^{\dagger n} a_i^n + \epsilon_n^b b_i^{\dagger n} b_i^n) + \sum_{\langle i,j\rangle}\sum_{n,m} t(a_i^{\dagger n} b_j^m + b_i^{\dagger n} a_j^m + a_i^{\dagger n} a_j^m + b_i^{\dagger n} b_j^m), \qquad (2.2)$$

where ϵ's depend on the chosen spin as suggested by Fig.2.4. We have replaced $c \to a$ or $c \to b$ so that a_i and b_i belong to the same i'th unit cell, indices n, m go over all the orbitals, and i, j go over all the unit cells in the lattice. The notation has also been truncated, since all the terms in the second sum should in fact have their own

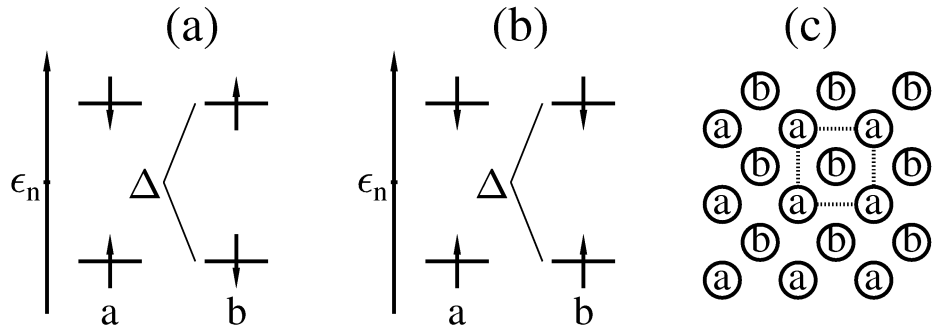

Figure 2.4: The level scheme for a given shell n with the energy ϵ_n. (a) shows the antiferromagnetic case (with $\epsilon_n^a = \epsilon_n^b \pm \Delta$, depending on spin), (b) the ferromagnetic case (with $\epsilon_n^a = \epsilon_n^b$ for both spins) and (c) shows the square lattice, the unit cell and the notation for for the dots in a unit cell. The square lattice is *bipartite*, i.e. there is only $a \leftrightarrow b$ hoppings present.

hopping integrals $t_{i,j}^{n,m}(a,b)$, because whether the symmetry sets the integral to zero or not, must be checked for all cases separately and may depend on all the indices.

The Method

The magnetic ground state of a QD lattice for given N and t is determined as follows. First the system is assumed to be F or AF, and the energy parameters in Eq.(2.2) are chosen accordingly from Fig.2.4 for fixed Δ, Δ_{sd} and t. The band structure $\epsilon_n(\boldsymbol{q}, \{t, \Delta, \Delta_{sd}\})$ is obtained easily by taking the eigenstates to have a Fourier-transformed form $|\psi\rangle = \sum_{ik} \exp(i\boldsymbol{q} \cdot \boldsymbol{r}_i)(\alpha_k |a_i^k\rangle + \beta_k |b_i^k\rangle)$.

Since the gaps between the main shells are large, much larger than Δ or Δ_{sd}, all the dynamics of the system concentrate on the valence shell and the full core electrons as well as the empty shells can be neglected. This allows the numerical calculation of the band structures for all the shells separately. An example of the band structure for a one-dimensional QD chain is shown in Fig.2.5.

For a given N, which is the sum of spin-up and spin-down electrons, the ground state magnetic phase, either F or AF, is then determined by the smaller total energy, i.e. the sum of the single-particle energies up to ϵ_F.

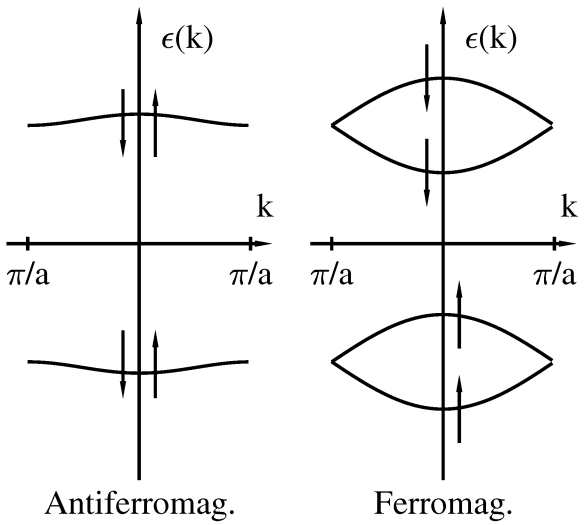

Figure 2.5: The band structures for AF (left) and F (right) systems in $1D$ linear chain with $1s$ symmetry, where $\epsilon = 0$, $\Delta = 1$ and $t = 0.2$. The AF bands are always spin-degenerate and F bands have a stronger dispersion due to smoother potential.

Analysis of the Results for a Square Lattice

Performing the calculations as explained above leads to the main results shown in Fig.2.6, which can be directly compared to the results of the DFT calculations presented in Fig.2.2.

It is seen that, indeed, the model exhibits the same systematics: half-shell antiferromagnetism, partly filled or nearly full shell ferromagnetism and filled shell nonmagnetism. The half-filled shell AF can be explained at certain level with the help of the band structure of Fig.2.5. Because the ferromagnetic exchange potential is flat, the bands have a strong dispersion, and with small occupation F systems have smaller total energy than AF systems. As N increases, the F system starts to occupy the upper bands whereas the AF system keeps occupying the same band, because it is spin-degenerate. If the two lowest bands of Fig.2.5 are filled, corresponding to half-filled shell, the AF system ends up with a smaller total energy.

Notice that N is any fractional number, so that all the cases with integer N, as in Fig.2.2, are just singular lines in the phase diagram. One also has to remember that here a smaller t corresponds to larger a, and because in reality the outer orbitals correspond to larger spatial extent, the same t for outer orbitals corresponds to larger lattice constants in real space as compared to inner orbitals. Furthermore, one cannot

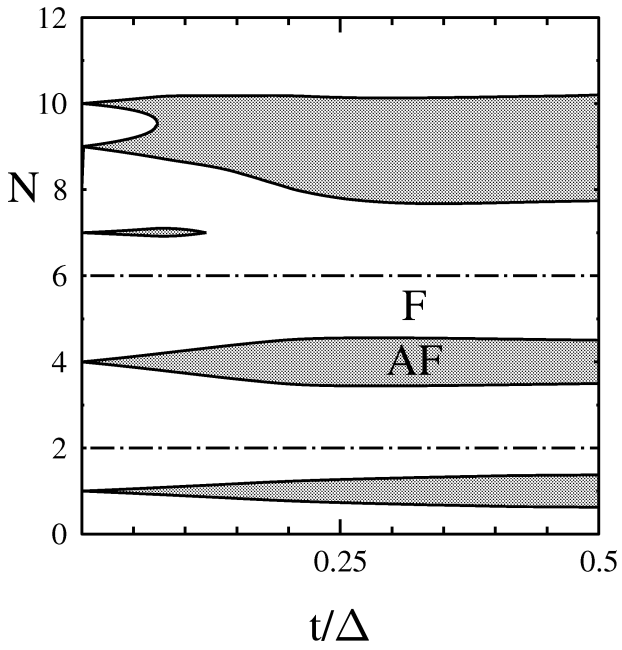

Figure 2.6: The magnetic phase diagram of a square QD lattice calculated using the TB model. N is any fractional number from 0 to 12, the dash-dotted line denotes full shells and t is plotted in units of Δ. The grey color denotes antiferromagnetic (AF) regions whereas white regions are ferromagnetic (F). All the t's are the same for all the nearest-neighbour orbitals, unless hopping is forbidden by symmetry. $2s-1d$ splitting is chosen as $\Delta_{sd}/\Delta = 1/2$.

expect to see any of the features of small a (or, more precisely, large overlap), because the whole argumentation of the tight binding method would in that case eventually break down.

This simple TB model seems to explain the magnetic behaviour surprisingly well, considering the following deficiencies. The exchange splitting Δ is taken to be independent of the electron number, though more realistically one should expect Δ to get larger with the shell filling as there are more electrons interacting with each other. In addition, the calculations of Koskinen *et al.* suggest that Δ is different for each orbital. However, one can think that the monotonic variation $\Delta = \Delta(N)$ as well as the (mostly) monotonic variation of t with a are already taken into account in the single parameter $t(a)/\Delta(N)$. Due to these monotonic variations the qualitative form of the phase diagram cannot change if we calculate all the overlap integrals $t = t(a)$ and plot the diagram with N and a instead, at least for s and p-shells. The filling of the sd-shell brings forth the parameter Δ_{sd}/Δ, which cannot be estimated in a simple way. If $\Delta_{sd}/\Delta \gg t/\Delta$, the s and d orbitals behave as two distinct shells, as there

is not much hopping between them, and the system shows mid-2s-shell and mid-1d-shell antiferromagnetism separately. This is why we see AF regions at $N = 7, 10$ with any Δ_{sd}/Δ for a small t. With small Δ_{sd}/Δ the AF area vanishes with increasing t when the bandwidth increases and gets bigger than Δ_{sd}/Δ, because the ferromagnetic bands arising from d-states, due to the stronger dispersion, come sufficiently down to remove the mid-2s-shell AF completely.

Beyond Square Lattices

Apart from just verifying the existing results for a square lattice, it is easy to do calculations for other lattices as well. Fig.2.7 shows the same phase diagram for s and p shells as Fig.2.6, but now including hexagonal (triangular) and honeycomb lattices as well. The results are basically the same as for a square lattice, as no dramatic changes are even expected, only the shapes of the AF regions are slightly different. The antisymmetry with respect to the mid-shell of the hexagonal lattice is only due to the fact that the lattice is not bipartite, i.e. there are $a \leftrightarrow a$ and $b \leftrightarrow b$ hoppings present. Note that although hexagonal lattice is frustrated and one might expect it to favour ferromagnetism, it actually displays mid-shell antiferromagnetism to the largest extent.[1] This can be explained by the large coordination number of the hexagonal lattice in the following way.

An enlargement of the 1s-shell phase diagram with small t is shown in Fig.2.8, which suggests that a larger lattice coordination number c leads to a wider area of mid-shell AF. This can be realized in the following way. By having a D-dimensional cubic lattice and orbitals with 1s symmetry, the band structure can be relatively easily obtained to be

$$\epsilon(\boldsymbol{q}) = \frac{1}{2}(\epsilon_a + \epsilon_b) \pm \frac{1}{2}\sqrt{(\epsilon_a - \epsilon_b)^2 + 4t^2|A(\boldsymbol{q})|^2}, \tag{2.3}$$

where $A(\boldsymbol{q}) = \sum_i^{n.n.} e^{-i\boldsymbol{q}\cdot\boldsymbol{r}_i}$ is the sum over all the phase factors of different nearest neighbour hoppings. In band minima the wave vector is near π/a or zero, so that $|A(\boldsymbol{q})| \sim c$, and by expanding for small t the energies of band minima go as

$$\begin{cases} \epsilon \approx -\Delta/2 - (ct)^2/\Delta & \text{, for AF case} \\ \epsilon \approx -\Delta/2 - ct & \text{, for F case.} \end{cases} \tag{2.4}$$

Thus the AF band minimum becomes the lower one with $t/\Delta > 1/c$; a larger coordination number widens the AF area with a small t. This vague argumentation relied on the cubic symmetry of the lattice and on the 1s symmetry of the occupied orbital. For other orbitals the symmetry may prevent hopping in some directions, but as compared to the 1s-symmetry this prevention may be viewed just as a reduction to a kind of 'effective' coordination number that takes into account only the allowed

[1] In hexagonal lattice the antiferromagnetic phase consists of parallel lines of alternating spin.

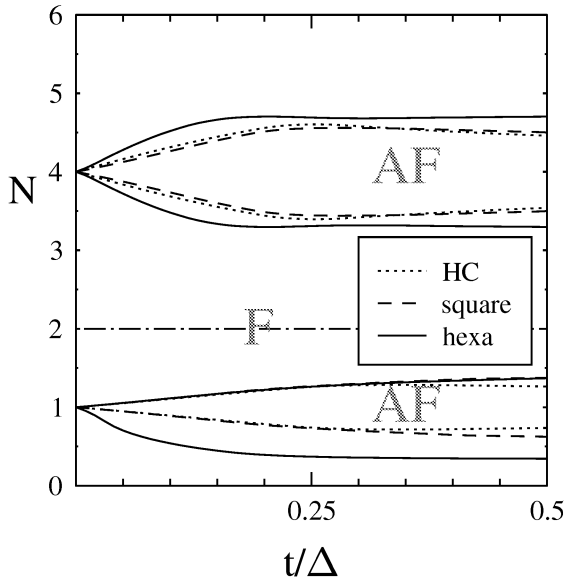

Figure 2.7: The magnetic phase diagram for $1s$ and $1p$ orbitals for honeycomb(HC,dotted line), square(dashed line) and hexagonal(solid line) lattices. The lines separate F and AF regions.

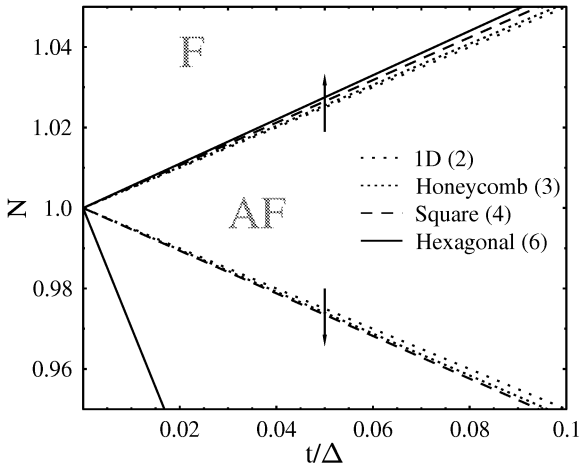

Figure 2.8: An enlargement of the $1s$-shell magnetic phase diagram of Fig.2.7 showing the coordination number effect. The numbers in parentheses are the coordination numbers and the arrows indicate the direction of increasing coordination number. For completion we have also included 'linear lattice', i.e. an array of $1D$ linear chains with $c = 2$ (the band structure of which is actually shown in Fig.2.5).

nearest-neighbour hoppings. For non-cubic lattices such as the hexagonal or honeycomb lattices the justification is not as evident, but there is no clear reason to expect a dramatic deviation from this coordination number effect.

This predicted effect remains to be justified at least with a systematic DFT approach, although preliminary results already support it. Otherwise this simple TB model seems to work surprisingly well, despite the known deficiencies. Many of these could be remedied by treating t's and Δ's more rigorously, but that would just complicate the model unnecessarily, and one would not expect the results to even get considerably different.

3 Quantum Rings and the Heisenberg Model

The Heisenberg model, describing the interaction of localized electrons, is one of the basic models in condensed matter physics. The interaction, electrostatic in nature, is represented as the interaction between the spins of localized electrons, and results in a very clear and intuitive form for the Hamiltonian operator. This chapter introduces the Heisenberg model and explains the way it appears to the description of quantum rings in the form of a model Hamiltonian. This discussion is devoted to publications I and II, where we studied quantum rings in a perpendicular magnetic field in terms of the model Hamiltonian.

3.1 The Heisenberg Model

Spin Model of Electrostatic Interactions

Consider two well-separated, localized electrons on states $\varphi(\boldsymbol{r}-\boldsymbol{R}_{1,2}) \equiv \varphi_{1,2}(\boldsymbol{r})$ and a spin-independent Hamiltonian. If the states are singly occupied, the possible anti-symmetric two-body wave functions with $S_z = 0$ are

$$\Psi_{\pm}(\boldsymbol{r}_1, \boldsymbol{r}_2) \propto [\varphi_1(\boldsymbol{r}_1)\varphi_2(\boldsymbol{r}_2) \pm \varphi_1(\boldsymbol{r}_2)\varphi_2(\boldsymbol{r}_1)] \times [\chi_\uparrow(1)\chi_\downarrow(2) \mp \chi_\uparrow(2)\chi_\downarrow(1)], \tag{3.1}$$

with the upper signs giving spin-singlets and the lower signs spin-triplets. Calculating the Coulomb interaction energies, one ends up having different energies on $\Psi_\pm$ because of the different symmetry in the spatial part. The direct magnetic interactions are much weaker than the electrostatic interactions, but it is via the exchange of particle coordinates that the strong electrostatic interaction is manifested by the spin-arrangement of the system [35]. For this reason the *spins* are blamed for the interaction, referred to as the exchange interaction, and the energy difference of the triplet-singlet states is called the exchange splitting. With this reasoning one can *construct* the Heisenberg Hamiltonian [36, 37]

$$\hat{H} = -J \sum_{\langle i,j \rangle} \boldsymbol{S}_i \cdot \boldsymbol{S}_j, \tag{3.2}$$

where the summation $\langle i, j \rangle$ again refers to electron spins that are nearest-neighbours and the spin-operator $\boldsymbol{S}_i$ obeys the commutation relations for an angular-momentum operator $[S_i^\alpha, S_j^\beta] = i\delta_{ij}\epsilon_{\alpha\beta\gamma}S_i^\gamma$. The symbol J represents the exchange splitting and can have positive or negative signs leading to ferro- and antiferromagnetism for the localized spins, respectively.

The Heisenberg Hamiltonian (3.2) can be derived somewhat more convincingly from the Hubbard model, introduced in Sec.4.1. The connection between these two models has actually a very important role in the whole Thesis, but these matters are discussed in the next chapter.

Solving the Heisenberg Model

The Heisenberg model, and especially its simplified version, the Ising model, are one of the most studied models in physics in overall. Solving the full Heisenberg model has turned out to be quite challenging: as the ferromagnetic ground state is simply the state of parallel spins, the antiferromagnetic ground state is already much more difficult to solve [38, 39]. Numerical computations are easy for small systems and also mean field approach gives a rough description of the physics of the model [9]. For exact results in one dimension the technique of Bethe trial wave function, the Bethe *Ansatz* may be used. However, this way one ends up with a complex non-linear system of equations, that may generally be quite difficult to solve.

3.2 Model Hamiltonian for Narrow Quantum Rings

Rotational and Vibrational Spectra

Narrow quantum rings with few electrons were studied by Koskinen *et al.* [34], among others [40, 41]. Fig.3.1 shows the energy spectrum obtained from configuration-interaction calculations for six-electrons in the ring-potential (1.2) with the real-space Hamiltonian (1.3) [34].

One evident feature of the spectra is the energy increase with M, the total angular momentum, as M^2, and the spectrum is symmetric about $M = 0$. The different vibrational bands get more clearly separated for narrower rings. Every band also reveals a fine-structure that is related to the spin-structure. All these features are present in a model Hamiltonian suggested also in Ref. [34].

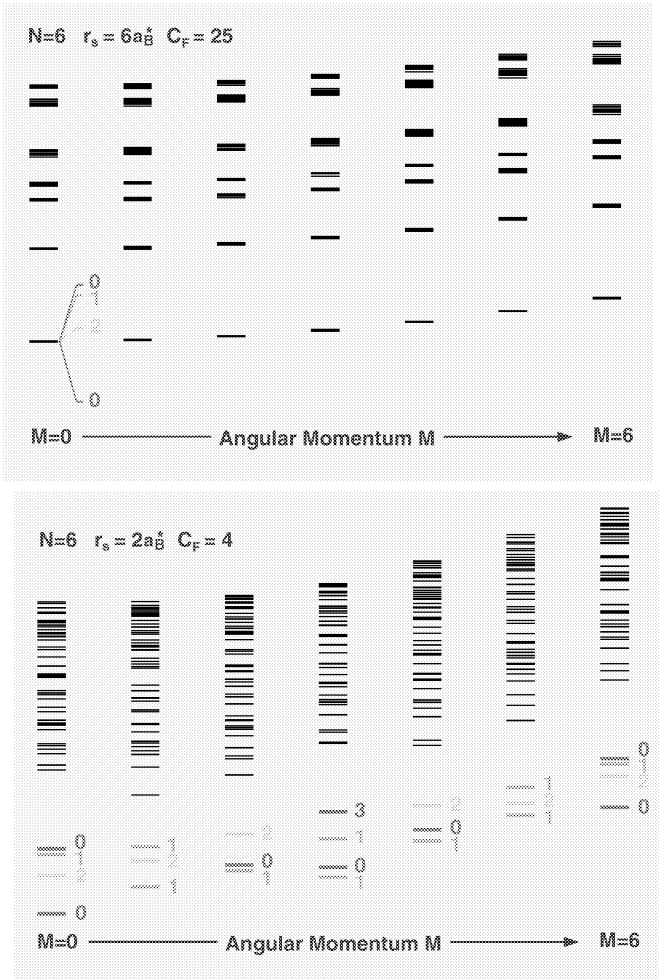

Figure 3.1: The energy spectrum of a six-electron system in a quantum ring potential (1.2), calculated with the CI method for two different radial confinements [34]. The numbers indicate the total spin of the state. The upper panel is a narrow ring and it shows several vibrational bands, whereas the lower panel is a wider ring and the vibrational bands come down in energy. The parameter C_F in the figures measures the height of the first radial excitation energy to the one-dimensional Fermi-energy, i.e. $\omega = C_F \hbar \pi^2/(32mr_s^2)$, where the ring radius $R = Nr_s/\pi$. The Bohr radius a_B^* is written in effective mass units. The expansion of the spin-states for the narrow ring and $M = 0$ indicates that the spin-structure in both rings is the same.

The Model Hamiltonian

The CI results presented above were found to be extremely well described by the following model Hamiltonian

$$\hat{H} = \frac{\hbar^2}{2I}\boldsymbol{M}^2 - J\sum_{\langle i,j\rangle}\boldsymbol{S}_i \cdot \boldsymbol{S}_j + \sum_{\alpha}\hbar\omega_\alpha \hat{n}_\alpha, \tag{3.3}$$

which can be understood as follows. Since the radial confinement is strong, the electrons cannot pass each other easily and thus end up localized in their internal frame of reference, forming a Wigner molecule [42]. This N-electron system therefore rotates as a *rigid rotator*, giving the first term in the Hamiltonian, where I is the moment of inertia of the rotator ($I \sim NmR^2$) and $\boldsymbol{M} = M\hat{z}$.[1] Internally localized electrons interact via the exchange interaction and give rise to the second term, where the negative coupling constant J depends on the ring parameters. Notice especially that the antiferromagnetic Heisenberg model is used even though the electrons are not localized by an external confinement. However, despite the 'localization' the electrons can still vibrate about their internal equilibrium positions. They have vibrational eigenmodes in the internal frame, resulting in the last term, where $\hbar\omega_\alpha$ turned out to be the energies of the *classical* vibrational eigenmodes α.

Comments About the Model Hamiltonian

The model is fairly accurate in strong radial confinement, i.e. in *quasi*-one-dimensional rings, but becomes less accurate in more shallow rings, because the system gets more two-dimensional and the analog with the $1D$ rigid rotator is demolished.

The one-dimensionality of the ring can be characterized by the parameter C_F that measures the height of the first radial excitation energy to the non-interacting $1D$ Fermi energy, i.e. $C_F = \hbar\omega/[\hbar^2\pi^2/(32m^*r_s^2)]$, where the ring radius $R = Nr_s/\pi$ and r_s is the one-dimensional density parameter. Because the exchange splitting J comes from the overlap between the localized electrons, one expects the splitting to get smaller as the system becomes more one-dimensional (C_F increases), because then the electrons are more strongly repelled and the overlap is diminished. The splitting is also expected to get smaller with smaller N (larger r_s) for the very same reason. In the lowest vibrational band the product of the parameters I and J in the range $2 \le r_s \le 6$ and $2 \le C_F \le 25$ can be accurately described by the relation [I]

$$IJ = [0.273 + 0.004(r_s^2 C_F) + 2.24 \times 10^{-6}(r_s^2 C_F)^2]^{-1}, \tag{3.4}$$

[1] Note that in two-dimensions $\boldsymbol{L} = \boldsymbol{M} \equiv L_z\hat{z}$, and consequently the eigenvalues of $\boldsymbol{L}^2$ have the form l^2, not $l(l+1)$.

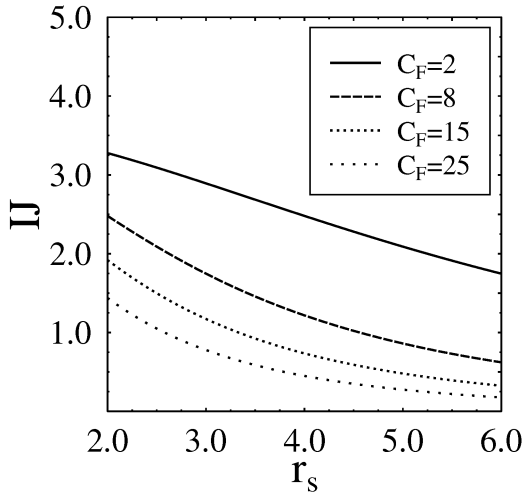

Figure 3.2: The function (3.4) plotted for r_s for a few values of C_F. Larger r_s (smaller density) and larger C_F (more strict one-dimensionality) both decrease the effective J, as anticipated.

plotted as a function of r_s in Fig.3.2 for a few values of C_F. It is seen that J indeed gets smaller for larger r_s and larger C_F.

Note also that it is not sufficient to merely solve the Heisenberg Hamiltonian (3.2) for the N-electron ring and add up with the other terms in the Hamiltonian (3.3) blindly, because all the eigenstates of the Heisenberg Hamiltonian have to have the correct symmetry corresponding to the angular momentum M. The angular momenta of the eigenstates of Heisenberg rings must be revealed by using the symmetry operations and character table of the group C_{Nv}.

3.3 Analysis of the Model Hamiltonian

In this section we review publications I and II and analyze the Model Hamiltonian (3.3) in more detail by numerical calculations. The eigenstates of Heisenberg rings (3.2) were computed by standard FORTRAN IMSL library routines, and could be performed quickly in a home computer. The main emphasis is on the behaviour of the rings in the presence of a perpendicular magnetic field.

Inclusion of a Magnetic Flux

In the presence of a perpendicular magnetic field $\boldsymbol{B} = B\hat{z}$ it is easy, rather than to perform the CI calculations all over again for all the different values of B, to use the model Hamiltonian, since the inclusion of $\boldsymbol{B}$ into the model is straightforward.

From the minimal substitution or from the second order perturbation theory one can get the energy shift of a state with given M as

$$\Delta E_M = \langle \Psi_M | \Delta H_B | \Psi_M \rangle = \frac{e^2}{8mc^2} B^2 R^2 N + \mu_B B M + g \mu_B B S_z, \tag{3.5}$$

because all the many-body states have M and S_z as good quantum numbers. We denote $\mu_B = e\hbar/(2mc)$ as the Bohr magneton and g as the Landé g-factor. We have neglected the fact that the rotating molecule might not have exactly the radius R, but rather a slightly larger radius due to rotation induced expansion [41].

We can write the magnetic flux piercing the ring as $\phi = \pi R^2 B$. The Landé g-factor for a free electron would have the value $g = g_0 \approx 2.0023$, but since inside a semiconductor the effective Landé factor for conduction electrons is different, we consider a general value of $g = 0 \ldots 2$. Approximating the rigid electron system by the classical moment of inertia $I = NmR^2$ and turning into atomic units, we can write the model Hamiltonian (3.3) with a magnetic field as

$$\hat{H} = -J \sum_{\langle i,j \rangle} \boldsymbol{S}_i \cdot \boldsymbol{S}_j + R^{-2} \left[\frac{1}{2N} \left[M + N \left(\frac{\phi}{\phi_0} \right) \right]^2 + g S_z \left(\frac{\phi}{\phi_0} \right) \right] + \sum_\alpha \hbar \omega_\alpha \hat{n}_\alpha, \tag{3.6}$$

where $\phi_0 = h/e$ is the flux quantum. From Eq.(3.6) one can easily see that the only effect of the magnetic field is to 'tilt' the energy spectrum (Fig.3.1) so that the minimum energy state corresponds always to the angular momentum $M \sim -N(\phi/\phi_0)$. By tilting we mean that making ϕ more negative the right-hand side of the parabolas with larger M is pushed downwards and the left-hand side with smaller M is lifted upwards. If $g \neq 0$ also the spin-degeneracy is lost by dragging the states with a large S_z downwards.

Vibrational States

The trickiest part of the model consists of the vibrational modes which have to be put in 'by hand'. The energy ratios of the classical vibrational eigenmodes have to be calculated and adjusted to the quantum mechanical spectrum with group-theoretical tools. It is obvious that the vibrational states do not play any role in the ground state

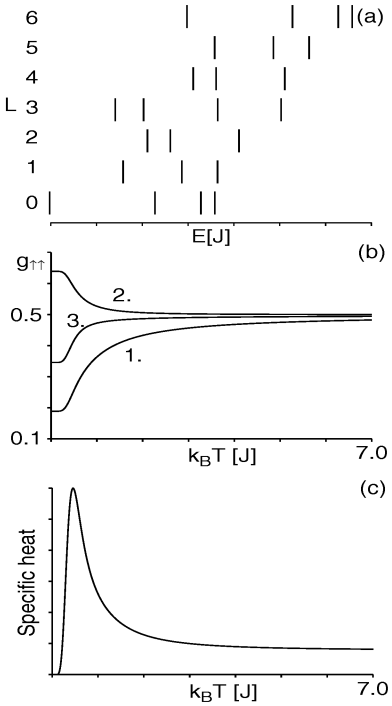

Figure 3.3: (a) The energy spectrum of $N = 6$ ring with $IJ = 6$ and vibrational states neglected. The spectrum is rotated in order to get the energy axis horizontal. (b) Pair correlation functions $g_{\uparrow\uparrow}(d)$ with the numbers indicating the value of d (for definition, see text) and (c) specific heat in finite temperatures. By comparing (b) and (c) to (a), we see that the main structures vanish already in temperatures corresponding the first excited states.

properties of the system, not even in non-zero magnetic fields, but might affect the finite-temperature properties of various quantities.

Fig.3.3 shows the specific heat and the pair correlation functions for a six-electron ring in zero magnetic field. The specific heat shows a finite peak above the ground state that is due to the large degeneracy of the lowest-lying excited states, and becomes constant soon after that within the temperature range $k_BT \sim 5J$. It is worthwhile to mention that the width of the bands, i.e. the range of the spin-splitting, denoted by Δ_J, is given by $\Delta_J \sim J \times N/2$, and hereby one can conclude that the specific heat becomes constant in temperatures comparable to the fine structure of the rings. The pair-correlation function, defined as

$$g_{\sigma\sigma'}(d) = \langle \hat{n}_{i,\sigma} \hat{n}_{i+d,\sigma'} \rangle, \tag{3.7}$$

also shows radical behaviour only below temperatures corresponding to the first ex-

cited states. The correlations get smaller with greater distances d and indicate antiferromagnetic order, as expected. The fact that the correlations vanish already at low temperatures indicate that the strong AF order and the internal symmetries between the ground state and the lowest excited states are considerably different. If the same quantities are plotted in a non-zero magnetic field, all that is expected to be found is some quantitative change in the form of the curves.

By means of the examples above one may conclude that the vibrational states are not important in finite-T properties of QRs where the model is valid. The narrower the ring, the larger the parameter C_F, and the higher the vibrational bands are compared to the spin-splitting, i.e. $\hbar\omega \gg \Delta_J$. If temperatures of the order $k_BT \sim \hbar\omega$ are reached, the thermodynamic quantities already have a covering average over the lowest vibrational band and no additional features are brought about when higher vibrational states get populated. These are the main reasons why the vibrational states within the validity range of the model are neglected altogether in the following discussion.

Persistent Current with $g = 0$

Persistent current (PC) has always been an interesting quantity to study in one-dimensional systems. It is an equilibrium current that arises when an Aharonov-Bohm flux pierces the ring and drives the electrons to form a current, even if the magnetic field would just go through the ring center and avoid areas where the electrons actually are [43, 46]. For rings one can quite generally derive the relation for PC as $I(\phi) = -\partial F/\partial\phi$, where F is the free energy of the system [44, 45]. In particular, the periodicity of the persistent current as a function of ϕ in zero temperature is reflected via the ground state energy periodicity.

Fig.3.4 shows the ground state energy periodicity, and consequently also the persistent current periodicity, of the Hamiltonian (3.6) as a function of the coupling constant J with $g = 0$, which corresponds just to the 'tilting' of the parabolas like the ones in Fig.3.1. Clearly, with $J = 0$ there is no spin-splitting[2] and the ground state changes N times from $M = 0$ to $M = N$ as $\phi = 0 \to \phi_0$ resulting in the periodicity ϕ_0/N, as seen also in Fig.3.5(d) with $g = 0$ [22]. If we increase the coupling constant J, the states for given M with different spin are split, and by tilting the spectrum we may skip some values of M and result in larger periodicity. By this we mean that while the period may not be exactly ϕ_0/N (except for $J = 0$), the energy still shows N peaks in the range $\phi = 0 \ldots \phi_0$, and hereby e.g. the peaks in Fourier-transformed spectrum indicate ϕ_0/N-periodicity [V]. In the extreme of very large J, if the ground state of the Heisenberg ring is non-degenerate with $S = 0$, one obtains the periodicity ϕ_0 corresponding to the shift of ground-state angular momenta in steps of N. With

[2]The upper panel of Fig.3.1 could be seen as having $J \approx 0$.

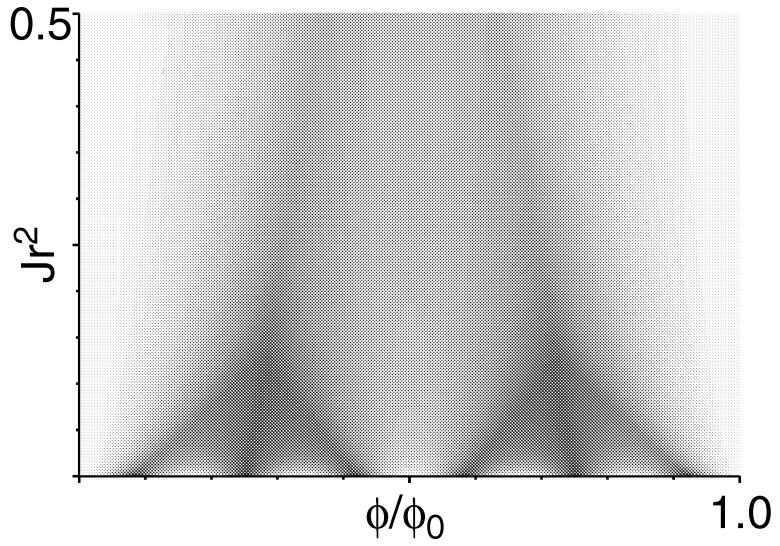

Figure 3.4: The ground-state energy of a six-electron ring as a function of ϕ and J with $g = 0$. Darker areas denote higher energies. The periodicity ϕ_0 can be seen to develop soon outside the picture with J greater than 0.5. (Actually the vertical axis is $|J|r^2$, since $J < 0$.)

intermediate J the periodicity $\phi_0/2$ is obtained, as would happen in the lower panel of Fig.3.1.

If we now refer to Eq.(3.4), we may conclude that the periodicity of the persistent current changes from $\phi_0 \rightarrow \phi_0/2 \rightarrow \phi_0/N$ as the effective J decreases and the ring gets narrower.

The Zeeman Effect, $g \neq 0$

Experimentally it might be quite difficult to confine the magnetic field so that it would penetrate just the interior of the ring and not couple to the spins of the electrons at all.

Fig.3.5 shows the spin and angular momentum phase diagrams as a function of the magnetic flux and the effective Landé g-factor for two different values of IJ. Looking at the angular momentum phase diagrams for $J = 0$ and small g one can see that the periodicity ϕ_0/N is recovered, but as there is no spin-splitting, a larger g makes the Zeeman energy to pick the state with a larger S_z. In the end with maximum g, the state with $S_z \sim N/2$ is picked, and since that state appears only with angular momenta in

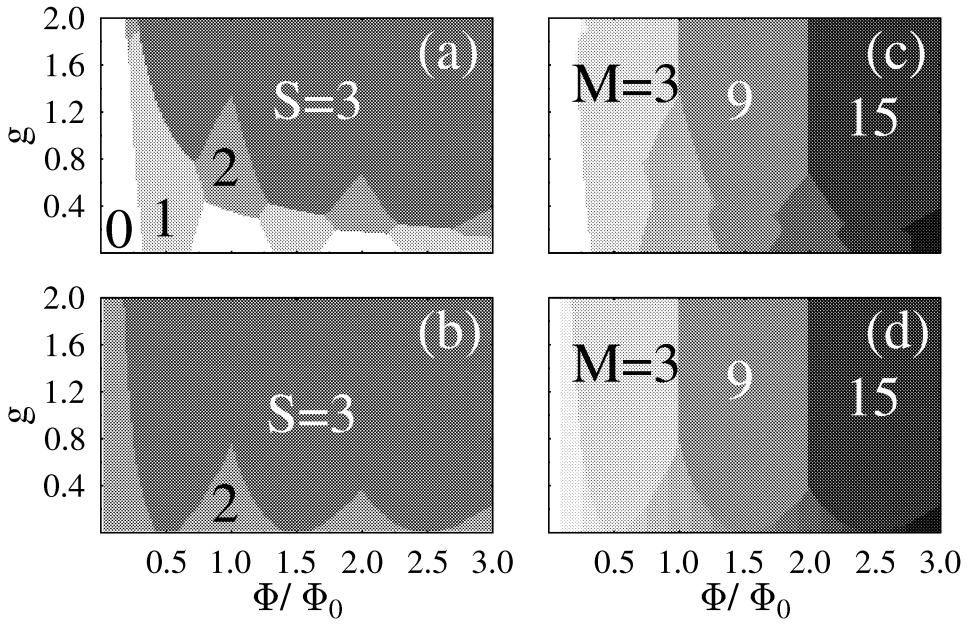

Figure 3.5: The ground-state spin (left-hand side) and angular momentum (right-hand side) phase diagrams for six-electron ring for two values of IJ. In upper diagrams (a) and (c) $IJ = 1.8$, and in lower diagrams (b) and (d) $IJ = 0$. For $IJ = 0$ the spin states are degenerate exactly only for $g = 0$.

steps of N, the result is the period ϕ_0. If J is increased, the state with $S_z \sim N/2$ is put higher in energy due to antiferromagnetism, and it requires a larger g (or ϕ) to get this state to be the ground state. This can be seen also in the spin phase diagrams. With small g the antiferromagnetism wins and the total spin remains small until the system becomes polarized for large enough g or ϕ, and returns the periodicity ϕ_0.

To see the effect of the temperature to the phase diagrams of Fig.3.5, one should just look at them from a distance or screw up one's eyes, because nothing new is brought about to the general features already shown. This blurring to the extent where the periodicity vanishes happens at temperatures of the order of $k_B T \sim J$.

This completes the short introduction to the analysis of the model Hamiltonian (3.3) in the presence of a magnetic field. However, the concepts developed and the phenomena observed in this chapter are further processed in the first part of the next chapter, as we study quantum rings from another point of view and with another model, the Hubbard model.

4 Quantum Rings, Coupled Quantum Dots and The Hubbard Model

In this chapter we study the ability of the Hubbard model to describe quantum rings and coupled quantum dots by reviewing the main results of publications III, V and VI. Especially the study of quantum rings will form a complementary point of view to what was described in the last chapter in the framework of the model Hamiltonian, Eq.(3.3).

4.1 The Hubbard Model

The Hamiltonian Operator

The standard form of the Hubbard Hamiltonian can be derived quite readily starting from Eq.(1.7). First we assume only one band, i.e. one state per site. In the non-diagonal hopping part we apply the same approximation as in the tight binding model, which was that only nearest-neighbour hopping is considered by assigning $t_{ij}^{nn'} \equiv -t$ if i and j are nearest neighbours. The electron-electron interaction, however, is not neglected, but since we only have one state per site, the electrons occupying the same site are forced to have an opposite spin, and we may denote $V_{\sigma\sigma'}^{nn'mm'} \equiv \delta_{\sigma\neq\sigma'} \times U$. With these approximations the standard form of the Hubbard Hamiltonian takes the form

$$\hat{H} = -t \sum_{\langle i,j\rangle,\sigma} c_{i,\sigma}^{\dagger} c_{j,\sigma} + U \sum_{i} \hat{n}_{i,\uparrow} \hat{n}_{i,\downarrow}, \tag{4.1}$$

where $\hat{n}_{i,\sigma} = c_{i,\sigma}^{\dagger} c_{i,\sigma}$ is the number operator for an electron at site i with spin σ [47, 48, 49, 53].

In short, the Hubbard model describes electrons hopping in a lattice of sites with the hopping amplitude t, while they always pay an energy penalty U whenever a site is doubly occupied by opposite spins. Usually the parameter t is set equal to one, in which case one can continually study the effect of interactions by varying U. It is the

competition of the physically two very different processes that makes the physics of the Hubbard model surprisingly rich and diverse: The first term is trying to keep the electrons in motion whereas the second term tries to keep them apart. The ratio of the number of electrons to the number of states available, called *filling*, becomes relevant since the importance of the contact interaction term depends on how frequently the electrons actually interact.

Connections to Other Models

The diversity of the Hubbard model has certain consequences. Instead of deriving the Hamiltonian (1.7) in the introduction chapter, we could have actually derived the Hubbard model straight away, because it is the *generic model* for all the lattice models presented in this Thesis. However, we preferred to use Eq.(1.7), since a more general Hamiltonian was required in Chap.2.

As already mentioned in previous chapter, the Heisenberg model has an especially important connection to the Hubbard model, and it can be summarized in the following way. If the two parameters of the Hubbard model satisfy $U \gg t$ and the number of electrons equals the number of sites, i.e. the system is half-filled, one would anticipate having one electron on each site. Starting from the extreme with $t = 0$, this state is also a multiply degenerate ground state of the system with each site singly occupied and no hoppings. With a finite but small t the first term of operator (4.1) can be considered as a perturbation for the second one and treated by the standard perturbation theory. The correction is of second order and the result can be cast into the form of Eq.(3.2) with the relation $J = -4t^2/U$, where t^2 refers to the second order and U^{-1} to the energy of the virtual doubly occupied site [52].

The half-filled Hubbard model thus reduces to the AF Heisenberg model in the limit $U \gg t$. This is intuitive, because while large U localizes electrons, there is still some hopping as long as the Pauli principle does not prevent it; the hopping activity — and the energy reduction — is at its largest when the hopping is always allowed, which is the case in AF configuration with opposite spins in nearest-neighbour sites.

The tight binding model is obtained readily[1] by setting $U = 0$, and the so-called *t-model* is obtained with $U = \infty$, which also is related to the Hubbard model with totally polarized electrons or 'spinless fermions'. The $t - J$*-model* is a combination of the hopping term and the Heisenberg term, so that the hopping electrons, instead of

[1] This happens only virtually for the Hamiltonian, since the basis set for the Hubbard Hamiltonian consists of many-electron states, whereas the TB basis set consists of single-particle states.

experiencing a direct Coulomb (on-site) interaction, feel the nearest-neighbour exchange interaction. All these models are closely related and one model can be derived from another model in suitable limits [3, V].

Solving the Hubbard Model

Despite the apparent simplicity of the Hamiltonian (4.1), it remains extremely difficult to solve in the general case. The dimension of the basis increases as $\binom{L}{N_\uparrow}\binom{L}{N_\downarrow}$, which restricts the exact numerical diagonalization to very small systems. Mean field theory can even give qualitatively incorrect results [2], whereas some exact results, especially for the one-dimensional chain, may require quite heavy mathematical machinery [50].

In the publications studied in this chapter the eigenstates of (4.1) have been solved mainly by the exact diagonalization method using standard FORTRAN IMSL and LAPACK library routines. In paper V the Bethe Ansatz technique was also used. Note that in Eq.(4.1), without any Zeeman splitting, it is in fact sufficient to consider the case $N_\uparrow = N_\downarrow$ for N even or $N_\uparrow = N_\downarrow \pm 1$ for N odd, since then S_z would be minimum and yield the whole energy spectrum. All the other possibilities for $N_\uparrow$ and $N_\downarrow$ would yield just the degenerate states with different S_z.

4.2 Ideal Hubbard Rings

Since the typical QR potential (1.2) is smooth, the electrons are not externally localized to certain points in the ring. However, as the model Hamiltonian for quantum rings, Eq.(3.3), suggests, the electrons are localized in their internal frame of reference while rotating in the laboratory frame of reference as a rigid rotator. This way considered the Hubbard model might not be as invalid in describing electrons in a QR as one might first think [51]. In this section we review the main results of publication V, where we studied, among other things, the Hubbard model in ideal quantum rings. These results, and the results of the next section, have also a central role in the whole Thesis.

Relation to the Model Hamiltonian

In the last section we argued how the Hubbard model turns into the Heisenberg model with half-filling and $U \gg t$. However, if we want to use the Hubbard model to describe rotating electrons in a ring, the system must be less than half-filled if U is large; in

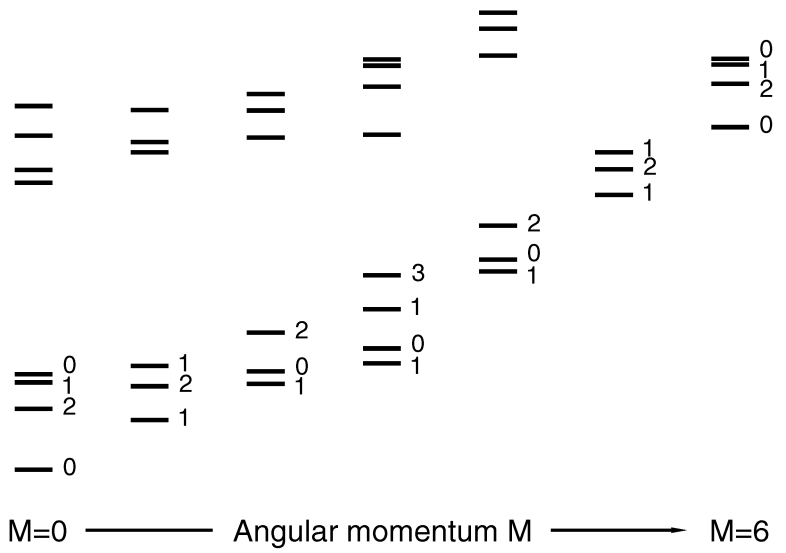

Figure 4.1: The many-body energy spectrum of an ideal Hubbard ring with $N = 6$ and $L = 8$ with $U = 40$. Note the obvious similarity with the original rotational and vibrational energy spectrum shown in the lower panel of Fig.3.1, obtained using the CI method.

an exactly half-filled system the electrons would be localized also in the laboratory frame. Surprisingly only a single empty site enables a free rotation of the electrons and hence also persistent currents.

Fig.4.1 presents the many-body spectrum of an ideal Hubbard ring with $N = 6$, $L = 8$ and $U = 40$, as a function of the total angular momentum M. By comparing with the rotational and vibrational spectrum of Fig.3.1, one can see the obvious similarity. The spin structure obtained is *exactly* the same as given by CI calculation or by the model Hamiltonian. This indicates that the connection to the antiferromagnetic Heisenberg model is conserved, even though the system is less than half-filled. In addition, the energy rises as M^2, so the Hubbard model also witness the rigid rotation of the electron system. It is rather remarkable that this kind of simple lattice model is able to reproduce all these effects!

The connection to the Heisenberg model can be further analyzed. If we remove the M^2-contribution from the total energy, and appropriately scale the energy spectra of the Hubbard model, we are able to see that it approaches even more accurately that of the Heisenberg ring as the number of empty lattice sites is increased, as long as U is sufficiently large. Only now the relation between the model parameters is smaller than the usual $J = -4t^2/U$ of the half-filled case, and depends on the number of empty sites $J = J_{eff}(L)$, with J getting smaller with more empty sites [58]. The U and L

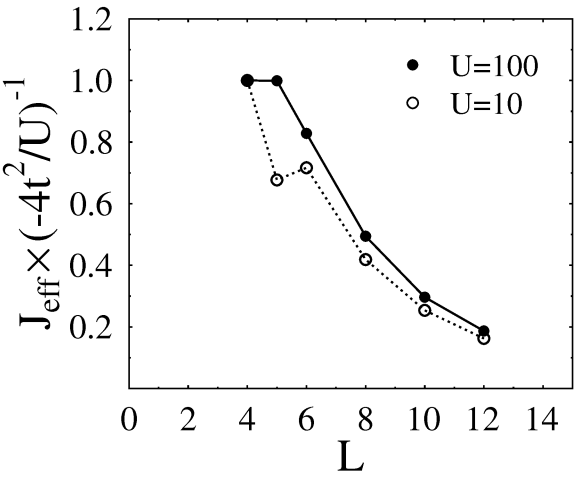

Figure 4.2: The L and U-dependence of the effective exchange coupling constant J_{eff} for $N = 4$. The black dots are the values determined from the exact solution for $U = 100$ and the white ones for $U = 10$. With $L = 4$ the system is half-filled and the antiferromagnetic coupling constant is $J = -4t^2/U$, as usual. Compare with Fig.3.2, where we have a similar behaviour if we identify U with C_F and r_s with L. (Note that since energy axis is scaled with $-4t^2/U$, J_{eff} is indeed smaller with $U = 100$.)

dependence of J_{eff} for the $N = 4$-system is depicted in Fig.4.2. Note especially the similarity shared with Fig.3.2, which shows the effective J of the model Hamiltonian (3.3) as a function of C_F and r_s.

Persistent Currents

The magnetic field, which is the driving force of the PC, can be introduced into the Hubbard model as a simple phase factor in the hopping integral, as indicated by Eq.(4.2) in the next section. Fig.4.3 now shows the energy spectrum of a Hubbard ring with a few discrete values for U, plotted as a function of the magnetic flux going from from $\phi = 0$ to $\phi = \phi_0$ for every value of U. The length of the ring is $L = 8$ and the number of electrons $N = 4$, with $N_\uparrow = N_\downarrow = 2$. Referring again to the relation between the ground state energy and the persistent current in zero temperature, we can see that the periodicity of the persistent current decreases from ϕ_0 with $U = 0$ to ϕ_0/N with $U = 1000$ via the intermediate periodicity $\phi_0/2$ [54]. This is similar to the periodicity change obtained by the model Hamiltonian (3.3), because there we obtained a shorter periodicity as the ring got narrower and J decreased (see Fig.3.4). This is very satisfactory, because we can think that the non-interacting case $U = 0$ corresponds to a very shallow ring where the electrons can pass each other from large

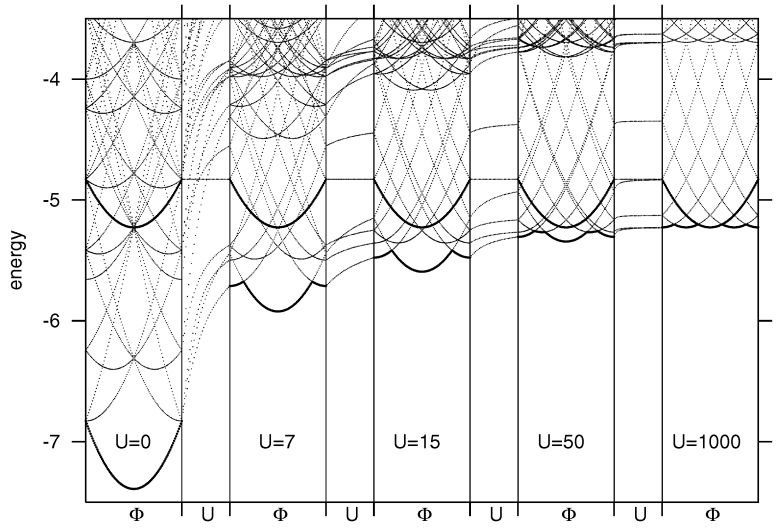

Figure 4.3: Magnetic flux and U dependence of the many-body spectra of a Hubbard ring with $L = 8$ and $N_\uparrow = N_\downarrow = 2$. Flux goes always from zero to ϕ_0 and U increases in between with $\phi = 0$. The lowest energy state and the lowest state with $S = 2$ are shown in bold lines. The state with $S = 2$ is independent of U since the electrons are already polarized and cannot occupy same sites anyway due to the Pauli principle.

distances, whereas the strongly interacting case $U \to \infty$ corresponds to a very narrow ring, where the rotating electrons have to pass each other at very short distances thus interacting and repelling one another effectively.

Vibrational States?

By adding more empty lattice sites to the ring incorporates also other effects than the renormalized Heisenberg J. Fig.4.4 presents the effect of adding lattice sites from $L = 4$ to $L = 8$ with $N = 4$ and $U = 40$. When one increases the number of empty lattice sites from one to many, there appears higher bands that can in fact be identified as the *vibrational* modes of the rotating electrons, the similar kind of vibrational modes as the ones present in the model Hamiltonian and shown for example as the higher bands in Figs.3.1 or 4.1. One can plausibly arrive at this identification using the Bethe Ansatz technique in the limit of infinite U.

The essence of the vibrational states may be simply illustrated by the case of polarized, non-interacting electrons in a strictly $1D$-ring. The one-particle states have the form $\psi_i(\varphi) \propto e^{im_i\varphi}$, where the quantum numbers $\{m_i\}$ are the single-particle

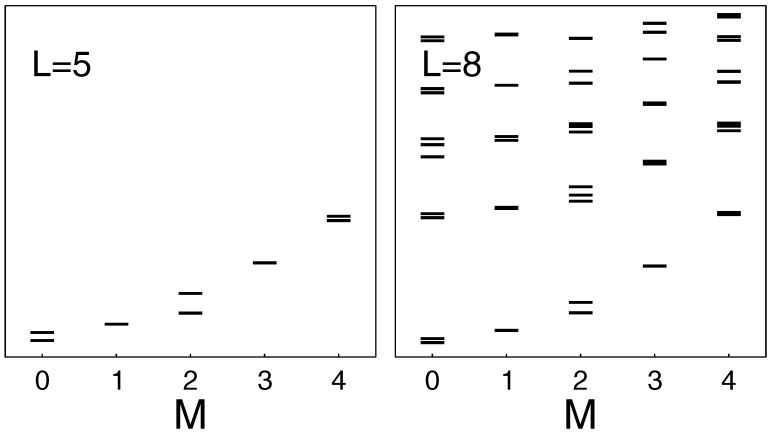

Figure 4.4: The energy spectra of Hubbard rings with $N = 4$ and $U = 40$ for $L = 5$ (left panel) and $L = 8$ (right panel). With a single empty site there is only one band (vibrational ground state), but with more empty lattice sites we get increasing number of vibrational bands above the lowest band. Compare the right panel especially to the upper panel of Fig.3.1, which shows the vibrational bands of a very narrow QR.

angular momenta. One can make the many-body Slater determinants by selecting a set of m_i's to give the total angular momentum $M = \sum m_i$. Just by looking at the internal structure of the Slater determinants via correlation functions, one can find resemblances to the rigid rotation, but also to the classical vibrational eigenmodes of the N-electron system. For a non-interacting system! This is naturally due to the fact that fermions cannot pass each other in a strictly $1D$-ring: If we introduce larger gaps in the set of single-particle angular momenta[2] $\{m_i\}$, we also give large differences to the 'velocities' of the electrons, and because of that they bump into each other harder and start vibrating more vigorously. This is not quite the frame in the Hubbard model, but may shed light to this interpretation of vibrational modes. And after all, the Hubbard model with $U = \infty$ is just the (lattice) model of polarized electrons because the electrons are not allowed to be at the same site.

In this section we have gained confidence toward the fact that the Hubbard model could actually describe the rigid rotation of the N-electron system, give the internal structure related to the Heisenberg model and even give a signature of the vibrational bands. All these features are completely consistent with the physical picture provided by the model Hamiltonian (3.3). This encourages us to apply the Hubbard model even further and study rings beyond the ideal $1D$-case.

[2]If initially the quantum numbers m_i consist of consecutive integer numbers.

4.3 Small, Imperfect Hubbard Rings

In the real world it would seem quite unrealistic to think that experimentally studied quantum rings could be completely clean and without any impurities [15, 55]. It is then of great importance to study how impurities alter the properties of ideal $1D$ quantum rings. In this section we review the results of publication VI, where the effect of impurities in small Hubbard rings was studied more profoundly.

Using small Hubbard rings and exact diagonalization it is actually very easy to introduce imperfections at non-perturbative level to the perfect ring symmetry. As compared to other methods, because of the broken symmetry, analytical as well as some exact numerical (continuum) methods can become quite tedious. The drawback of the exact diagonalization method is that we must restrict ourselves with a few electrons in a ring of length $L \lesssim 12$, whereas we might want to study also bigger rings. At this point, however, we note that the Hubbard model does not necessarily compare better to the 'real' model Hamiltonian as the number of lattice sites is increased [58]. This is because, as long as there are empty sites, the contact interaction really matters only when the electrons overlap, and these processes only become scarce with increasing L. This is to say that only the energy scale diminishes with larger L, as is suggested also by Figs.3.2 and 4.2, but the physics of the system does not appreciably change.

Models for Impurities

For treating the impurities we insert an additional term to the original Hubbard Hamiltonian (4.1), so that the impurity Hamiltonian reads

$$\hat{H} = -\sum_{\langle i,j\rangle,\sigma} t_{ij}(e^{-i(2\pi/L)(\phi/\phi_0)}c^\dagger_{i\sigma}c_{j\sigma} + H.c.) + U\sum_i \hat{n}_{i\uparrow}\hat{n}_{i\downarrow} + \sum_{i,\sigma}\epsilon_i\hat{n}_{i\sigma}. \tag{4.2}$$

We allow for different hopping integrals t_{ij} and site-dependent on-site energies ϵ_i. The presence of the magnetic field manifests itself through a phase factor that modifies the hopping integrals [57]. Note that the phase factors appear only in hoppings along the ring circumference of length L, and vanish if the hop is in radial direction. With this Hamiltonian and exact diagonalization it is relatively easy to study the effects of single impurities, random impurities, electric field and also the temperature to the persistent current I induced by the magnetic flux ϕ. As compared to previous studies related to the same subjects, this method allows an exact treatment of strong, non-perturbative impurities, and especially the inclusion of many-body effects, which we can study by continuously increasing the electron-electron interaction U [56, 59, 61].

In Fig.4.3 we saw how the periodicity of the persistent current decreased as the Hubbard U increased. When U is changed with a fixed ϕ, the resulting function $I(U)$ might

properly represent the effect of interactions to the persistent current, as long it does not contain any discontinuities that arise from the periodicity change. Among many other authors we use the representative value of $\phi = 0.25\phi_0$ for the magnetic flux and study the functions $I_{\phi=0.25\phi_0}(X, U)$, where X represents some impurity strength [59].

Persistent Currents in the Presence of Impurities

We study first a single impurity site for $L = 7$, $N_\uparrow = N_\downarrow = 2$ system with $X = \epsilon_1$. The resulting behaviour of the persistent current, $I(\epsilon_1, U)$, is shown in Fig.4.5(a). For $\epsilon_1 = 0$ one can immediately notice the decrease in the current with increasing U [60, 61, 62]. This comes from the fact that larger interaction makes the electrons to move less independently in the lattice and ultimately only rotation as a rigid rotor is possible; naturally the rotation is easiest when electrons with the opposite spin do not interact at all. With increasing ϵ_1 the current decreases, whereas the effect of U is first to slightly increase, but later to slightly decrease the current. When the impurity is attractive, $\epsilon_1 < 0$, the current behaves in a bit more subtle way, and ends up having a local maximum whenever $\epsilon_1 + U = 0$. This is because if the impurity-localized electron has, say, a spin up, the spin-down electrons do not feel the impurity potential *at all* and can circle around the ring quite freely.

This interpretation can be studied further by considering an odd number of electrons, as in Fig.4.5(c) and (d), so that the system is not symmetric with respect to the different spins anymore. The overall form of the total current, $I = I_\uparrow + I_\downarrow$, is like in Fig.4.5(a), but the separate spin-components are quite different, and even have opposite signs. This surprising discrepancy in the direction of the current can be fortunately explained simply by the model of non-interacting electrons in a $1D$-continuum ring. Impurity decreases both currents, while the interaction couples them and forces them to flow more in the same direction. In this situation, as we have only $N_\downarrow = 1$, the spin-up current is even larger with $\epsilon_1 + U = 0$ than with zero impurity (and the same U), because if the only spin-down electron is localized, the potential for the spin-up current is totally flat.

Also other kind of impurities, such as an electric field, characterized by the potential difference $X = V_E$ at the ring extremes, and especially a random potential, characterized by its width $X = W = \max(\{\epsilon_i\}) - \min(\{\epsilon_i\})$ with random ϵ_i, introduce similar kind of localization effects as ϵ_1. Generally speaking, the current decays monotonically as a function of the impurity strength, but exhibits weak local maxima as a function of U, where the location of the maximum goes as $U \sim X$.

It is interesting to see what happens if electrons could really escape and hide somewhere outside the ring. This escape might mimic the processes in the presence of external leads leading to electron reservoirs. We try to imitate leads by adding a stub,

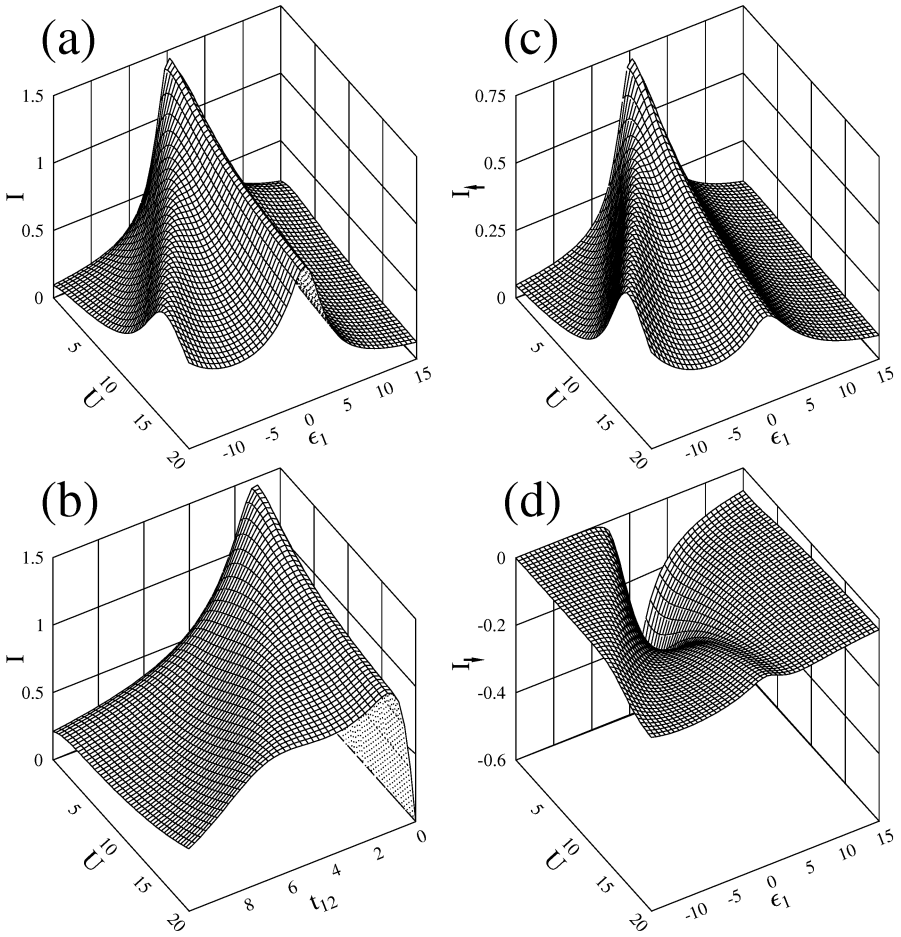

Figure 4.5: (a) $I(\epsilon_1, U)$ and (b) $I(t_{12}, U)$ for $L = 7$, $N_\uparrow = N_\downarrow = 2$, where t_{12} is the hopping integral between a single link in the ring with all the other t's equal to one. (c) $I_\uparrow(\epsilon_1, U)$ and $I_\downarrow(\epsilon_1, U)$ for $L = 7$, $N_\uparrow = 2$, $N_\downarrow = 1$. The magnitude of the flux is $\phi = 0.25\phi_0$.

a few extra lattice sites in the radial direction, outside the ring geometry. In Fig.4.3 we saw how the electron levels changed as a function of ϕ for a system with $N = 4$ and $U = 1000$, giving the ground-state periodicity ϕ_0/N, characteristic for a narrow ring. Fig.4.6 shows the same thing, but now with an inserted stub that consists of two lattice sites. It is clear that a periodicity of $\phi_0/3$ is obtained, *as if* the ring would contain only three electrons. By summing up the electron densities in the ring it can really be ensured that the stub completely localizes one electron and the rest of the electrons continue rotating in the ring without any disturbance from the stub [63]. This is not

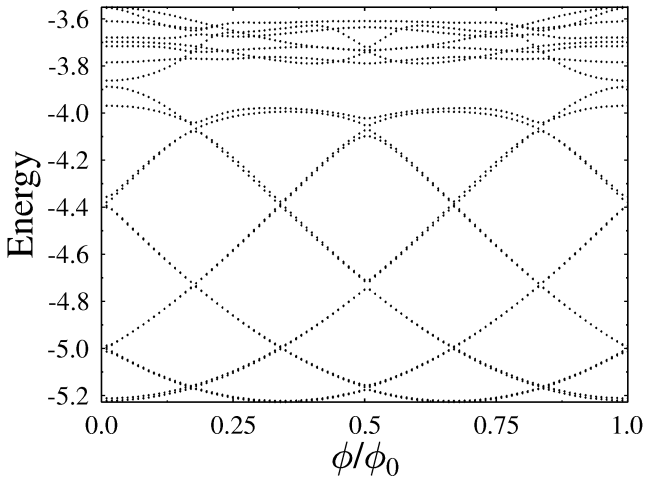

Figure 4.6: The ϕ-dependence of the many-body spectrum of a Hubbard ring for $L = 7$, $N = 4$ and $U = 1000$ with an additional stub with two sites. The ground state periodicity is $\phi_0/3 = \phi_0/(N-1)$, which suggests that only three electrons are participating in the current formation and one is completely localized in the stub. Compare especially with Fig.4.4, where the periodicity in an ideal ring with $U = 1000$ is ϕ_0/N.

the case if the length of the stub is e.g. one or three, because then the wave-function of the localized electron 'spills' into the ring, interfering with the rotating electrons and reducing the current considerably. The overall effect and importance of such an impurity depends crucially on the length and the form of the additional stub.

All the above results are valid in temperature $T = 0$. But as seen e.g. in Fig.4.6, the slopes $\partial E/\partial\phi$ of the excited states are frequently opposite to that of the ground state, which means that also the currents carried by those states have opposite signs. At least for perfect rings this results, after a flat region in the temperature scale set by the energy of the first excited state, in a very rapid decrease of the persistent current with increasing T [64].

Despite the apparent simplicity of the model, and the straightforward application to small Hubbard rings without any truly sophisticated method, it appears that most of the results given by the model in this section agree qualitatively very well with the most dedicated studies of quantum rings. This notion should not actually surprise us, especially after we already have seen how surprisingly well different models for one-dimensional systems may resemble each other.

4.4 Four-Wave Mixing in Coupled Quantum Dots

We end this chapter by studying something totally different, namely, coupled quantum dots in an optical experiment. A coupled QD is simply two QDs grown or fabricated next to each other, so that the dots, rather than being isolated, interact with each other in some manner. If the distance between them is large enough, so that the internal properties of the dots are not appreciably modified, the particles in the dots can be treated within the hopping scheme, and one convenient way to describe such a system is to use a Hubbard-type model. In this section we review the results of publication III, where certain optical properties of coupled dots were calculated using the Hubbard model. These properties are directly related to real quantities measured in a so-called four-wave mixing experiment, which can thus reveal information about the internal fine-structure of coupled QDs, even if the dots are embedded in a large inhomogeneously broadened ensemble.

A Hubbard Model for Coupled Quantum Dots

We start by considering an isolated QD with the following structure. We assume the ground state $|0\rangle$ to have no electrons or holes, but if a valence electron is promoted to the conduction band by an absorption of a photon in the visible region, an exciton $b_\sigma^\dagger|0\rangle$ is formed with an energy ϵ, where $b_\sigma^\dagger$ is the fermionic creation operator for an exciton with the electron spin σ. In the presence of a *bi*exciton $b_\uparrow^\dagger b_\downarrow^\dagger|0\rangle$, which means two co-existing excitons, the Coulomb correlations reduce the total energy to be $2\epsilon-\Delta$, where Δ is called the biexciton binding energy [70].

If now two such dots are brought close together, the electrons and holes start to hop and get delocalized in the two dots [65]. Fortunately it has turned out, that the exciton tunneling is preferred as compared to a separate electron and hole tunneling [69]. This allows us to treat the exciton as the elementary building block and to write the double-dot Hamiltonian as

$$\hat{H} = \epsilon \sum_\sigma (\hat{n}_{L\sigma} + \hat{n}_{R\sigma}) - t \sum_\sigma (b_{L\sigma}^\dagger b_{R\sigma} + b_{R\sigma}^\dagger b_{L\sigma}) - \Delta \sum_{i=L,R} \hat{n}_{i\uparrow}\hat{n}_{i\downarrow}, \qquad (4.3)$$

where L and R refer to 'left' and 'right' dots, respectively, and $\hat{n}_{i\sigma} = b_{i\sigma}^\dagger b_{i\sigma}$ [30]. Apart from the first term, which merely tells the number of excitons in the system ($\epsilon \sim$ eV $\gg \Delta \sim$ meV), Eq.(4.3) is nothing but the Hubbard Hamiltonian (4.1) with a negative interaction $U = -\Delta$.

The eigenstates of (4.3) can be solved analytically and are shown in Fig.4.7. Since the ground state is always the starting point and later we assume no other coupling to the

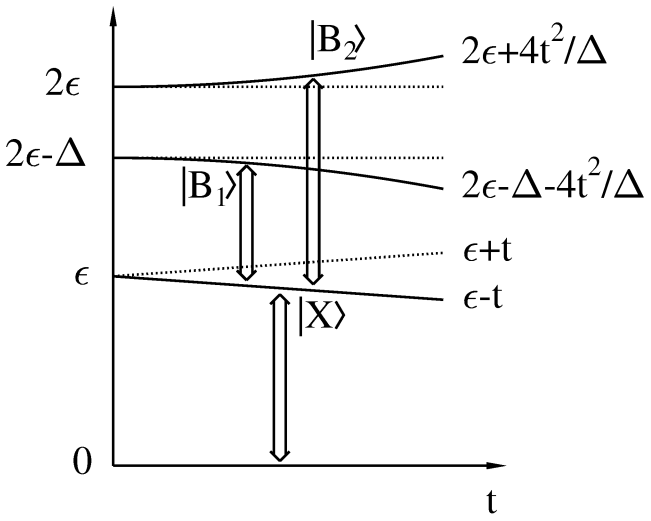

Figure 4.7: The level structure of a coupled QD obtained using the model (4.3) for small t. The arrows indicate the allowed optical transitions that can be reached starting from the ground state. X is the transition from the ground state to the state where a single exciton is delocalized in both the dots. B_1 denotes the transition from the state $|X\rangle$ to a state $|B_1\rangle$ where the excitons are *mainly* in the same dot, and B_2 denotes the transition to a state $|B_2\rangle$ where the excitons are localized mainly in different dots and where the biexciton binding energy is absent.

environment apart from the dipole coupling to the electromagnetic field, the dotted states can never be reached in optical transitions and can thus be totally ignored in our future computations.

At this stage we know the states $|i\rangle$ of our single coupled dot system. A convenient way to describe the state $|\psi(t)\rangle = \sum c_i|i\rangle$ of a whole ensemble of such coupled dots is the density matrix $\rho(t) = \sum c_i^* c_j |i\rangle\langle j|$. If the ensemble is inhomogeneous with a distribution of ϵ's, i.e. it is *inhomogeneously broadened*, the total ensemble can be described by many density matrices $\{\rho^l(t),\ l = 1, 2, \ldots\}$, all of which represent a smaller ensemble of dots, within which all the coupled dots have the same energy characteristics ϵ^l. The time evolution of $\rho^l(t)$ is governed by the Liouville-von Neumann equation and incorporates the coupling to the controlled laser field in the rotating-wave and dipole approximations, and the coupling to the electromagnetic vacuum responsible for the spontaneous emission of photons [74, 75]. The diagonal elements of ρ yield directly the occupations of the energy levels, and the off-diagonal elements describe the phase coherence between the levels. The off-diagonal elements also determine the (interband) polarization,

$$\mathcal{P}^l(t) = \sum_{i,j} \rho_{ij}^l(t) M_{ji}, \tag{4.4}$$

which is related to the emitted radiation from the sample. The quantity $M_{ij} = -e\langle i|r|j\rangle$ is the dipole-matrix element responsible for the electromagnetic coupling strength of the dipole transition between states i and j [10].

The Four-Wave Mixing Experiment

Optical measurements are in an important position in extracting information from nanoscopic structures. Visible light absorption with the photon energy in the electron-volt range can provide direct data about the discrete many-body level structure of an ensemble of quantum dots or quantum rings. In an inhomogeneous ensemble the fine structure of the individual dots in the meV range is often blurred in the direct absorption spectra by the large inhomogenious broadening in ϵ^l. In this section we introduce how this situation can be corrected.

If the occupation of the exciton and biexciton states of Fig.4.7 increase as a result of an intense laser pulse, the off-diagonal elements of ρ give non-zero interband polarization. The system then gradually decays into the ground state by spontaneous emission of light, with the photon energies corresponding to the allowed optical transitions. Because the transitions have different energies ($\sim \epsilon^l$ and $\sim (\epsilon^l - \Delta)$), the decaying signal undergoes beating corresponding to the energy differences in the transitions [68]. Fig.4.8 can be considered to illustrate this beating pattern for a single coupled dot or an ensemble with given ϵ^l. However, this beautiful beating pattern from the total ensemble gets blurred, since the off-diagonal elements evolve in time like $\rho^l_{ij} \sim e^{i\omega^l_{ij}t}$ and the relatively large differences in $\omega^l_{ij} \sim \epsilon^l/\hbar$ with different l, that are of the order of 30 meV, make the polarizations from different coupled dots to go quickly out of phase. From the blurred emission spectra one cannot see the beating patterns anymore, and consequently one cannot extract information about the fine-structure of the coupled dots. This situation can be corrected in a four-wave mixing (FWM) experiment.

The FWM setup consists of two consecutive short and intense laser pulses that are separated by a time delay τ and that travel in slightly off-parallel directions $\mathbf{k}_1$ and $\mathbf{k}_2$ as shown in the inset of Fig.4.8(a) [8, 71]. Without further justifications we state that this setup effectively causes the latter pulse, arriving at time $t = 0$, to 'reverse' the time development of the polarization induced by the first pulse, arrived already at time $t = -\tau$, so that at time $t = \tau$ each dot in the ensemble has the polarization again in-phase. The result is a delta-function-like photon echo pulse $S(t)$ in direction $2\mathbf{k}_2 - \mathbf{k}_1$ at time $t = \tau$ as shown in Fig.4.8(b) [72, 73].

Fig.4.8(a) shows the FWM signal from an isolated coupled QD or an ensemble with given ϵ^l. The beating frequencies would be the actual quantities of interest, but the signal vanishes in the total inhomogeneous ensemble because the polarizations go out of phase. If the inhomogeneity is only in ϵ's and not in Δ's or t's, the *beating frequencies*

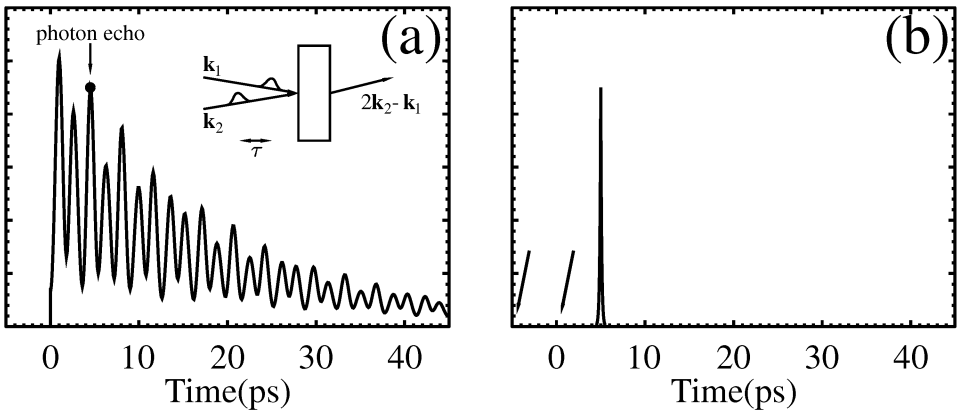

Figure 4.8: (a) The FWM signal $S(t)$ ($\tau \approx 0$) arising from a single coupled QD with the fast-oscillating $e^{i\epsilon^l t/\hbar}$part projected away (Heisenberg picture). The laser pulses excite the exciton and biexciton states which decay exponentially by spontaneous emission (here we have a short decay constant ~ 20 ps for clarity). The beating of the signal comes from the energy differences of the X, B_1 and B_2 transitions of Fig.4.7. The inset shows a schematic representation of the FWM setup. A short laser pulse is shot in the direction $\boldsymbol{k}_1$ at time $t = -\tau$ and at time $t = 0$ a second pulse of the same strength is shot in a slightly off-parallel direction $\boldsymbol{k}_2$. The result is an echo pulse in the direction $2\boldsymbol{k}_2 - \boldsymbol{k}_1$ at time $t = \tau$. (b) The two laser pulses with $t = \tau = -5$ ps and $t = 0$ are shown by the arrows and the peak at $t = \tau$ is the delta-function-like FWM signal $S(t)$ observed in the direction $2\boldsymbol{k}_2 - \boldsymbol{k}_1$ (while $I(\tau) = \int S_\tau(t)dt$ is the actual quantity measured). The width of the peak is related to the decay constant. The strength of the signal $I(\tau)$ measures the beating pattern of the individual coupled dots at time $t = \tau$, denoted by the filled circle in (a). Units are arbitrary.

still remain exactly the same in the whole ensemble. Thus Fig.4.8(a) represents the beating frequencies of the total, inhomogeneous ensemble, and the only problem that remains is to bring it forth experimentally.

In experiments the echo pulse is measured by the time-integrated signal $I(\tau) = \int S_\tau(t)\mathrm{d}t$ with a fixed τ. In Fig.4.8(a) the filled circle shows the moment of the echo signal for $\tau = 5$ ps; in every coupled dot in the total ensemble the echo signal takes place at the same point of the beating pattern and hence $I(\tau = 5$ ps) also shows a maximum. If $I(\tau)$ is measured systematically for many values of τ, the whole beating pattern is mapped out. This is how information about the fine-structure of coupled dots can be extracted from an inhomogeneously broadened ensemble. Numerically we calculate only $S(t)$ for a single coupled dot, or an ensemble with fixed ϵ^l, instead of $I(\tau)$ with multiple values of τ for the total ensemble.

We shortly mention that in numerics we do not need to take into account the spatial effects related to the directions of the laser and echo pulses. By following Ref. [66] we can take these into consideration by introducing phase differences in the two controlled

laser pulses, and the FWM-signal can be calculated from the interband polarization (4.4) in a straightforward manner.

Analysis of the FWM Signal

Fig.4.9 shows the modulus of the Fourier transformed signal $S(\omega) = \mathcal{F}[S(t)]$, which could equally well present the experimentally observed Fourier-transformed signal $I(\omega)$. The typical biexciton binding is $\Delta = 3\,\mathrm{meV}$ and the tunneling amplitude t goes from zero to ~ 1 meV. With $t = 0$ the coupled dot acts as two individual dots showing a beating frequency at 3 meV as expected. As t is increased, three different beating frequencies are identified: α corresponding to the beating between the transitions $X - B_1$, β between $X - B_2$ and γ between the transitions $B_1 - B_2$. It is notable that the α-peak gets bigger, whereas both β and γ get smaller with increasing t. The reason is that in α both the states X and B_1 are bonding states, the energy of which decreases with larger t. B_2 is an antibonding state, which results in smaller dipole-coupling to the X-state and consequently in weaker transitions and beatings against X- and B_1-transitions.

The level scheme of Fig.4.7, and thus the fine-structure of the coupled QD ensemble, can be quite readily constructed from the peak positions of Fig.4.9. Hereby the va-

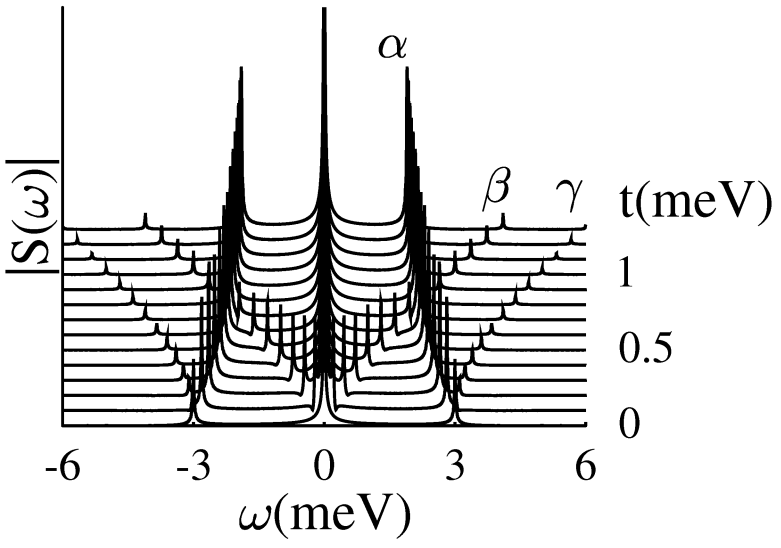

Figure 4.9: The final results for the FWM spectra of coupled QDs representing $|S(\omega)|$ for various values of t. The decay time is 500 ps.

lidity of the Hubbard-type model (4.3) could be directly tested. And, once more, we stress that all this information was extracted in the presence of the inhomogeneous broadening, larger than the fine-structure by an order of magnitude.

In this section we have demonstrated that the Hubbard model can be used also beyond the standard electron-tunneling approach. Although this topic is somewhat different in nature from the other subjects in this Thesis, it also shows how simple and straightforward it is to apply lattice models to describe semiconductor nanostructures.

List of Publications

I P. Koskinen, M. Koskinen, and M. Manninen, *Low-energy spectrum and finite temperature properties of quantum rings*, Eur. Phys. J. B **28**, 483-489 (2002)

II P. Singha Deo, P. Koskinen, M. Koskinen, and M. Manninen, *Fractional periodicity of persistent currents: A signature of broken internal symmetry*, Europhys. Lett. **63**, 864 (2003)

III P. Koskinen and U. Hohenester, *Four-wave mixing in coupled semiconductor quantum dots*, Solid State Comm. **125**, 529 (2003)

IV P. Koskinen, L. Sapienza, and M. Manninen, *Tight-Binding Model for Spontaneous Magnetism of Quantum Dot Lattices*, Physica Scripta **68**, 74-78 (2003)

V S. Viefers, P. Koskinen, P. Singha Deo, and M. Manninen, *Quantum rings for beginners: Energy spectra and persistent currents*, Physica E (in press)

VI P. Koskinen and M. Manninen, *Persistent Currents in Small, Imperfect Hubbard Rings*, Phys. Rev. B (in press)

The author has written papers IV and VI, the main part of paper I and a significant part of paper III, but merely assisted in writing paper V. The author has done the theoretical and numerical work in most of the publications, except in paper II, where he only made the numerical calculations, and in paper V, where he merely assisted in several topics.

5 Summary and Conclusions

The subject of this Thesis was to study the suitability of lattice models to describe the physics of semiconductor nanostructures. We studied the tight binding, the Heisenberg and the Hubbard models in quantum dot lattices, quantum rings and coupled quantum dots. The prevalent method was to solve the models with exact numerical diagonalization for small enough systems. The results were in fair agreement with previous studies, considering the relative simplicity of the models.

In chapter 2, where we reviewed the results of publication IV, we saw how a simple tight binding model was able to reproduce the qualitative behaviour of spontaneous magnetism of QD lattices. Remarkable enough, all the complex effects of exchange interactions were reasonably well described by postulating a single parameter, the exchange splitting Δ. This suggests that the underlying physical processes are not excessively complicated.

Publications I and II analyzed a previously suggested model Hamiltonian for narrow quantum rings. The model consists of a rotation of the rigid electron molecule, the spin-structure explained by the antiferromagnetic Heisenberg model, and vibrational modes explained simply by the classical vibrational eigenmodes. In chapter 3 we collected the main results of the model analysis, showing e.g. the irrelevance of the vibrational states, the persistent current periodicity change $\phi_0 \to \phi_0/2 \to \phi_0/N$ with increasing radial confinement, and the effect of Zeeman splitting to the ground-state properties.

Surprisingly enough, these very same phenomena were observed in quantum rings also by using the Hubbard model. The results of publications V and VI, reviewed in the beginning of chapter 4, indicated that the Hubbard model appropriately describes the Wigner-crystalline electron system in a narrow quantum ring. This gave us confidence to study quantum rings further by introducing imperfections to the perfect ring symmetry. And once more, the qualitative behaviour of persistent current in the presence of imperfections was in good agreement with earlier, more dedicated studies of the same subject. Generalizing even further, all the one-dimensional Hubbard model derivatives, the non-interacting and interacting electrons in $1D$-rings, as well as classical particles in a ring, share surprisingly many common properties, many of which are shown in the most sophisticated quantum-mechanical calculations.

At the end of chapter 4, we finally introduced a Hubbard -type model that was applied to describe exciton dynamics in coupled quantum dots. In publication III the model was used to predict quantities that would be directly experimentally accessible.

At this stage it seems that the Hubbard model derivatives capture the physics of nanostructures more essentially than what would be anticipated at first sight. The original purpose of these models was to describe electrons in localized atomic states, where some of the approximation might not work very well. However, in quantum dots the band structure confinement is not as steep as the Coulombic r^{-1}, and the bound states have smoother spatial format. This may lead to different character for the interaction of neighbouring sites. Furthermore, in quantum rings one can more easily achieve sufficiently low densities to form a Wigner molecule. All these factors may lead to the result that the lattice approximation work well in nanostructures.

The models have been mainly used to explain already familiar many-body phenomena of semiconductor nanostructures, although something new has also been observed. However, the main achievement of this Thesis has been to search and identify the general and dominating behaviour of interacting, nanoscopic many-electron systems. Thanks to the direct diagonalization and exact wave-functions, the physical processes are clearly visible and we obtain a clarity for the interpretation of results.

References

[I] P. Koskinen, M. Koskinen, and M. Manninen, *Low-energy spectrum and finite temperature properties of quantum rings*, Eur. Phys. J. B **28**, 483-489 (2002)

[II] P. Singha Deo, P. Koskinen, M. Koskinen, and M. Manninen, *Fractional periodicity of persistent currents: a signature of broken internal symmetry*, Europhys. Lett. **63**, 864 (2003)

[III] P. Koskinen and U. Hohenester, *Four-wave mixing in coupled semiconductor quantum dots*, Solid State Comm. **125**, 529 (2003)

[IV] P. Koskinen, L. Sapienza, and M. Manninen, *Tight-Binding Model for spontaneous Magnetism of Quantum Dot Lattices*, Physica Scripta **68**, 74-78 (2003)

[V] S. Viefers, P. Koskinen, P. Singha Deo, and M. Manninen, *Quantum rings for beginners: Energy spectra and persistent currents*, Physica E (in press)

[VI] P. Koskinen and M. Manninen, *Persistent currents in small, imperfect Hubbard rings*, Phys. Rev. B (in press)

[1] P. Harrison, *Quantum Wells, Wires and Dots* (Wiley, England 2000).

[2] M. P. Marder, *Condensed Matter Physics* (Wiley, New York, 2000)

[3] G. D. Mahan, *Many-Particle Physics* (Plenum Press, New York, 1981)

[4] P. L. Taylor and O. Heinonen, *Quantum Approach to Condensed Matter Physics*, (Cambridge Univ. Press, Cambridge, 2002)

[5] N. W Ashcroft and N. D. Mermim, *Solid State Physics* (Saunders, New York, 1976)

[6] D. Bimberg, M. Grundmann, and N. N. Ledentsov, *Quantum Dot Heterostructures* (Wiley, England, 1999)

[7] H. Bruus and K. Flensberg, *Many-body quantum theory in condensed matter physics* (lecture notes 2002)

[8] H. Haug, S. W. Koch, *Quantum Theory of the Optical and Electronic Properties of Semiconductors* (World Scientific, Singapore, 1990)

[9] C. Kittel, *Introduction to Solid State Physics* (Wiley, New York, 1996)

[10] M. O. Scully and M. S. Zubairy, *Quantum Optics* (Cambridge University Press, Cambridge, 1997)

[11] D. C. Mattis, *The Theory of Magnetism* (Harper & Row, New York, 1965)

[12] W. J. Caspers, *Spin systems* (World Scientific, Singapore, 1989)

[13] E. T. Yu, J. O. McCaldin and T. C. McGill, Solid States Physics: Advances in Research and Applications **46**, 1 (1992)

[14] S. Tarucha, D. G. Austing, T. Honda, R. J. van der Hage, and L. P. Kouwenhoven, Phys. Rev. Lett. **77**, 3613 (1996)

[15] A. Fuhrer, S. Lüsher, T. Ihn, T. Heinzel, K. Ensslin, W. Wegscheider, M. Bichler, Nature **413**, 822 (2001)

[16] H. Pettersson, R. J. Warburton, A. Lorke, K. Karrai, J.P. Kotthaus, J.M. García, P.M. Petroff, Physica E **6**, 510 (2000)

[17] A. Emperador, M. Pi, M. Barranco, and A. Lorke, Phys. Rev. B **62**, 4573 (2000)

[18] The Figures 1.3(a) and 2.1 are taken from the homepages of *Research Center for Integrated Quantum Electronics, RCIQE* (http://www.rciqe.hokudai.ac.jp/qcp/index.html). Fig.1.3(c) is from [15], Fig.1.3(d) from [33], and Fig.1.3(b) from the slide show *Quantum Dots* by Rajarshi Mukhopadhyay.

[19] M. A. Kastner, Physics Today **46**, 24 (1993)

[20] T. Chakraborty, *Quantum Dots: A Survey of the Properties of Artificial Atoms*, North-Holland, Amsterdam (1999)

[21] S. M. Reimann and M. Manninen, Rev. Mod. Phys. **74**, 1283 (2002)

[22] U. F. Keyser, C. Fühner, S. Borck, R. J. Haug, M. Bichler, G. Abstreiter, and W. Wegscheider, Phys. Rev. Lett **90**, 196601 (2003)

[23] L. Goldstein, F. Glas, J. Y. Marzin, M. N. Charasse, and G. Le Roux, Appl. Phys. Lett. **47**, 1099 (1985)

[24] P. M. Petroff, A. Lorke, A. Imamoglu, Physics today **54** (2001)

[25] G. L. Snider, A. O. Orlov, I. Amlani, X. Zuo, C. S. L. G. H. Bernstein, J. L. Merz, and W. Porod, J. Appl. Phys. **85**, 4283 (1999)

[26] T. Lundstrom, W. Schoenfeld, H. Lee, and P. M. Petroff, Science **286**, 2312 (1999)

[27] E. Pazy, I. D'Amico, P. Zanardi, and F. Rossi, Phys. Rev. B **64**, 195320 (2001)

[28] E. Biolatti, R. C. Iotti, P. Zanardi, and F. Rossi, Phys. Rev. Lett. **85**, 5647 (2000)

[29] D. Loss and P. DiVinzento, Phys. Rev. A **57**, 120 (1998)

[30] G. Burkard, D. Loss, and D. P. DiVincenzo, cond-mat/9808026 (1998)

[31] M. Koskinen, S. M. Reimann, and M. Manninen, Phys. Rev. Lett. **90**, 066802 (2003)

[32] K. Shiraishi, H. Tamura, and H. Takayanagi, Appl. Phys. Lett. **78**, 3702 (2001)

[33] A. Lorke, R. J. Luyken, A. O. Govorov, J. P. Kotthaus, J. M. Garcia, and P. M. Petroff, Phys. Rev. Lett. **84**, 2223 (2000)

[34] M. Koskinen, M. Manninen, B. Mottelson, S. M. Reimann, Phys. Rev. B **63**, 205323 (2001)

[35] W. Heitler and F. London, Z.Phys. **44**, 455 (1927)

[36] P. A. M. Dirac, Proc. R. Soc. London **A112**, 661 (1926)

[37] W. Heisenberg, Z. Phys. **49**, 619 (1926)

[38] H. Bethe, Z. Phys. **71**, 205 (1931)

[39] R. Orbach, Phys. Rev. **112**, 309 (1958)

[40] P. A. Maksym, Phys. Rev. B **53**, 10871 (1996)

[41] K. Niemelä, P. Pietiläinen, P. Hyvönen, and T. Chakraborty, Europhys. Lett. **36**, 533 (1996)

[42] E. Wigner, Phys. Rev. **46**, 1002 (1934)

[43] M. Büttiker, Y. Imry, R. Landauer, Phys. Lett. A **96**, 365 (1983)

[44] N. Byers and C. N. Yang, Phys. Rev. Lett. **7**, 46 (1961)

[45] F. Bloch, Phys. Rev. B **2**, 109 (1970)

[46] Y. Aharonov and D. Bohm, Phys. Rev. **115**, 485 (1959)

[47] J. Hubbard, Proc. R. Roc. London **266**, 238 (1963)

[48] J. Hubbard, Proc. R. Soc. London **A277**, 237 (1964)

[49] J. Hubbard, Proc. R. Soc. London **A281**, 401 (1946)

[50] E. H. Lieb, F. Wu, Phys. Rev. Lett. **20**, 1445 (1968)

[51] A. A. Zwyagin, Sov. Phys. Solid State **32**, 905 (1990)

[52] P. W. Anderson, Phys. Rev. **115**, 2 (1959)

[53] R. A. Broglia and J. R. Schrieffer, Proceedings of the international school of physics "Enrico Fermi" (Elsevier Science Publishers, Varenna, Italy, 1992)

[54] F. V. Kusmartsev, Phys. Rev. B **52**, 14445 (1995)

[55] U. F. Keyser, S. Borck, R. J. Haug, M. Bichler, G. Abstreiter, and W. Wegscheider, Semicond. Sci. Technol. **17**, L22-L24 (2002)

[56] B. S Monozon and P. Schmelcher, Phys. Rev. B **67**, 045203 (2003)

[57] R. E. Peierls, Z. Phys. **80**, 763 (1933)

[58] N. Yu and M. Fowler, Phys. Rev. B **45**, 11795 (1992)

[59] S. Viefers, P. Singha Deo, S. M. Reimann, M. Manninen, and M. Koskinen, Phys. Rev. B **62**, 10668 (2000)

[60] A. Müller-Groeling and H. A. Weidenmüller, Phys. Rev. B **49**, 4752 (1994)

[61] T. Chakraborty and P. Pietiläinen, Phys. Rev. B **52**, 1932 (1995)

[62] M. Kamal, Z. H. Musslimani, and A. Auerbach, cond-mat/9501122

[63] P. A. Sreeram and P. Singha Deo, Physica B **228**, 345 (1996)

[64] M. Büttiker, Phys. Rev. B **32**, 1846 (1985)

[65] G. W. Bryant, Phys. Rev. B **46**, 1893 (1992)

[66] L. Bányai, D. B. Tran Thoai, E. Reitsamer, H. Haug, D. Stainbach, M. U. Wehner, M. Wegener, T. Marschner, and W. Stolz, Phys. Rev. Lett. **75**, 2188 (1995)

[67] P. Borri, W. Langbein, J. Mørk, J. M. Hvan, F. Heinrichsdorff, M.-H. Mao, and D. Bimberg, Phys. Rev. B **60**, 7784 (1999)

[68] T. F. Albrecht, K. Bott, T. Meier, A. Schulze, M. Koch, S. T. Cundiff, J. Feldmann, W. Stolz, P. Thomas, S. W. Koch, and E. O. Köbel, Phys. Rev. B **54**, 4436 (1996)

[69] F. Troiani, U. Hohenester, and E. Molinari, Phys. Rev. B **65**, 161301 (2002)

[70] M. Bayer, O. Stern, P. Hawrylak, S. Fafard, and A. Forchel, Nature (London) **405**, 923 (2000)

[71] J. Shah, *Ultrafast Spectroscopy of Semiconductors and Semiconductor Nanostructures* (Springer, Berlin, 1996)

[72] M. Lindberg, R. Binder, and S. W. Koch, Phys. Rev. A **45**, 1865 (1992)

[73] A. Leitenstorfer, A. Lohner, K. Rick, P. Leisching, T. Elsaesser, T. Kuhn, F. Rossi, W. Stolz, and K. Ploog, Phys. Rev. B **49**, 16372 (1994)

[74] U. Hohenester, Solid State Comm. **118**, 151 (2001)

[75] U. Hohenester, F. Troiani, and E. Molinari in *Radiation-matter Interaction in Confined Systems*, edited by L. C. Andrean, G. Benedek, and E. Molinari (Soc. Italiana di Fisica, Bologna, 2002)